remote sensing

MDPI

Article

Characterization of an Active Fault through a Multiparametric Investigation: The Trecastagni Fault and Its Relationship with the Dynamics of Mt. Etna Volcano (Sicily, Italy)

Salvatore Alparone [1], Alessandro Bonforte [1], Salvatore Gambino [1], Sabrina Grassi [2,*], Francesco Guglielmino [1], Federico Latino [2], Gabriele Morreale [2], Graziano Patti [2], Laura Privitera [1], Francesco Obrizzo [3], Andrea Ursino [1] and Sebastiano Imposa [2]

[1] Istituto Nazionale di Geofisica e Vulcanologia, Osservatorio Etneo, Sezione di Catania, Piazza Roma, 2, 95125 Catania, Italy
[2] Dipartimento di Scienze Biologiche, Geologiche e Ambientali, Sezione di Scienze della Terra, Università di Catania, Corso Italia, 57, 95129 Catania, Italy
[3] Istituto Nazionale di Geofisica e Vulcanologia, Osservatorio Vesuviano, Sezione di Napoli, Via Diocleziano, 328, 80124 Napoli, Italy
* Correspondence: sgrassi@unict.it

Abstract: The Trecastagni Fault (TF) is an important tectonic structure in the middle-lower southern flank of Mt. Etna volcano. It is characterised by evident morphological slopes with normal dip-slip ruptures that directly affect roads and buildings. The TF plays a key role in the complex framework of the volcano dynamics since it represents part of the southern boundary of the unstable sector. Seismic surveys have been performed on three different areas of the fault to gain insights into the seismic stratigraphic structure of the subsoil. We considered the seismic activity of a sector of the territory affecting the surface evidence of the Trecastagni Fault in the period between 1980 and 2021 in order to highlight the main seismic release and define the space–time distribution of seismicity. Most of the seismicity is located in the north-western portion, while the central and southern sectors are characterised by low seismic activity. The strongest earthquakes occur mainly within the first 5 km of depth in the form of swarms and/or isolated shocks. Ground deformation techniques (levelling, In-SAR and two continuous extensometers) evidence a continuous aseismic slip of the TF that is interrupted by short accelerations accompanied by shallow seismicity. The Trecastagni Fault dynamics are strictly linked to magma pressurisation and intrusive episodes of Mt. Etna that induce additional stress and promote its slip along the fault plane. Multidisciplinary data analysed in this work, evidenced the dual behaviour of the fault, from aseismic creep to stick-slip, and the relation with magmatic activity, also suggesting the time delay in the response of the fault after the intense stress induced by dyke intrusion.

Keywords: flank dynamics; Mt. Etna volcano; Trecastagni Fault; DInSAR data; levelling network; MASW and HVSR surveys; impedance contrast sections

Citation: Alparone, S.; Bonforte, A.; Gambino, S.; Grassi, S.; Guglielmino, F.; Latino, F.; Morreale, G.; Patti, G.; Privitera, L.; Obrizzo, F.; et al. Characterization of an Active Fault through a Multiparametric Investigation: The Trecastagni Fault and Its Relationship with the Dynamics of Mt. Etna Volcano (Sicily, Italy). *Remote Sens.* **2022**, *14*, 4760. https://doi.org/10.3390/rs14194760

Academic Editor: David Gomez-Ortiz

Received: 2 August 2022
Accepted: 16 September 2022
Published: 23 September 2022

1. Introduction

Mt. Etna is among the most active volcanoes in the world and is considered one of the most interesting natural laboratories for the understanding of eruptive processes and the ascent of magma [1,2]. The geodynamics of Mt. Etna is dominated by the collisional process of the Eurasia and Africa plates, with a roughly N–S trend and an approximately E–W extensional regime. The volcano edifice is located at the intersection of the two major regional lithospheric lineaments, with NNW–SSE and NE–SW trends, which play a fundamental role in the dynamic processes of the volcano [1–4].

Recently, an imaging of Mt. Etna magmatic system has been proposed by De Gori et al., 2021 [5], by using time-lapse local earthquake tomography. They evidenced a deep reservoir,

broadly elongated between 4 and 9 km depth, as the principal volume of storage where primitive melts ascend directly from the mantle source that is connected with two shallower and smaller reservoirs directly feeding the summit craters activity. Volumes of shallow magma degassing and geometry of the conduits were imaged with locations of the tremor sources and of the long-period seismic events [6].

The complex interaction between regional stress, gravity force and dyke-induced rifting has led to the flank instability and slow sliding of the eastern and south-eastern flanks of the volcano [7–17]. Furthermore, the dynamic of eastern flank seems to have a key role in triggering volcanic eruptions, e.g., [18–20]. The eastern flank dynamics is confined by the Pernicana Fault System (Figure 1; PFS; [20–25]), which represents the northern boundary and, to the west, the N–S Ragalna Fault System (RFS; [26]). Conversely, the south-eastern boundary is less defined because the slip motion is distributed on different faults that progressively accommodate the sliding motion of the SE-wards sliding sector of the volcano, e.g., [10,11,27]. The South Fault System (SFS; Figure 1) represents one of the southern boundaries and is composed of two main parallel lineaments that include the Belpasso-Ognina and Tremestieri-Mascalucia faults and the San Gregorio and Aci Trezza faults [8,28–30]; (Figure 1). In some places, these faults are characterised by evident morphological slopes [31]. The Trecastagni Fault (TF) is a discontinuity extending along the southern flank of Mt. Etna, between the Trecastagni and San Giovanni la Punta villages, before joining the San Gregorio-Aci Trezza fault that also extends off-shore from the volcano [32,33]. The TF is an active structure with a roughly NNW–SSE trend (Figure 1), characterised by morphological escarpments and with a normal kinematic.

Ground deformation and dynamics of the TF have been investigated by medium-term satellite measurements that have estimated a slip rate of about 4–5 mm/year using Synthetic Aperture Radar (SAR) interferograms and Permanent Scatters techniques, with data starting from 1995 [27,28,30,34]. Similar results have been obtained after the installation of two extensometers along the TF in 2005 [8,31].

As reported in the study published by Azzaro et al., 2020 [35], for the Timpe Fault System (TFS), on the eastern slope of Etna, the slip along the TF can also occur by a continuous aseismic creep, as well as by occasional low-energy seismic crises, accompanied or not by transient acceleration of the dislocation.

The seismicity of the TF is characterised by very shallow earthquakes with typical focal depths of 1–2 km below sea level.

Several authors have highlighted feedback processes between magmatic events and flank movements at Mt. Etna, e.g., [15,18,19], suggesting that the slip of the TF may be encouraged by the edifice inflation, dyke intrusion and decollement slip [8]. The TF is of fundamental importance in the complex framework of the volcano because: (i) it is one of the structural lineaments sharing the southern boundary of the eastern flank; (ii) it generates ground deformation and seismic activity, also linked with the eruptive activity of the Mt. Etna volcano; and (iii) it is an important fault affecting the urban centre of a town on Mt. Etna, causing buckling in the existing buildings. Furthermore, during the last 40 years, seismic activity along the TF often occurs concurrently (e.g., 1983 and 1985 eruptions) or immediately before (e.g., 2002–2003, 2004–2005 eruptions) or after (2018 eruption) the main lateral eruptions of the volcano. During the 2018 Mt. Etna eruption, and after the 26 December earthquake (ML = 4.8; MW = 4.9) occurring along the Fiandaca-Pennisi Fault, a seismogenic structure belonging to the Timpe Fault System (TFS), the seismicity affected the central areas of the volcano and subsequently involved more peripheral sectors including the southern structures, in particular, the Tremestieri Etneo and Trecastagni Fault systems [36].

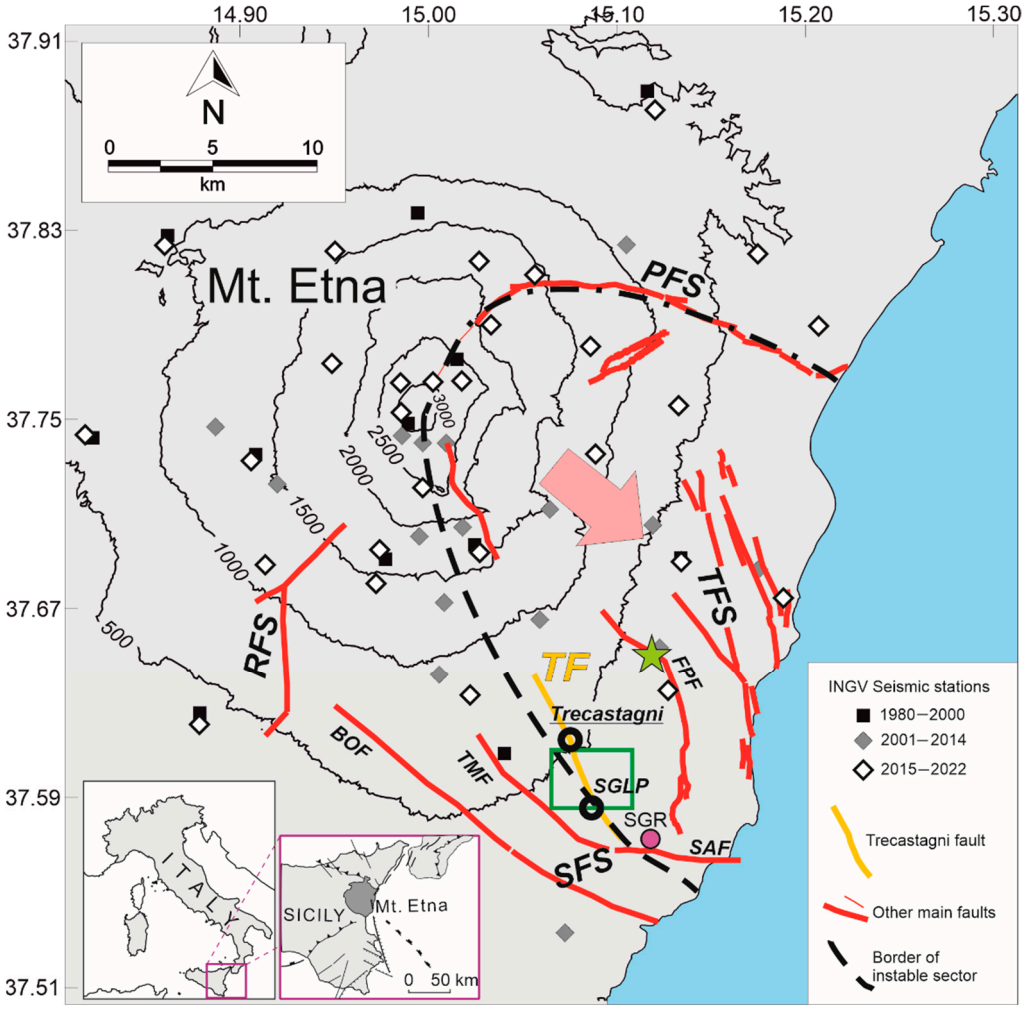

Figure 1. Map of Mt. Etna volcano and main tectonic elements from [34]. TFS: Timpe Faults System; PFS: Pernicana Fault System; TF: Trecastagni Fault; TMF: Tremestieri-Mascalucia Fault; BOF: Belpasso-Ognina Fault; FPF: Fiandaca-Pennisi Fault; SAF: San Gregorio-Acitrezza Fault; SFS: South Fault System; RFS: Ragalna Fault System; SGLP: San Giovanni La Punta. Seismic stations of the permanent (UNI-CT, IIV-CNR, INGV-OE) networks are indicated with black squares and grey and white diamonds, respectively (see text for details). Green star represents the ML = 4.8 earthquake recorded on 26 December 2018. SGR: S. Gregorio seismic station. Pink arrow: direction of sliding. Green square: study area. In the two insets (lower left side), a map of Italy and a schematic structural map of Eastern Sicily.

The aim of this paper is to carry out a characterization of this tectonic structure using a multidisciplinary approach at different time and space scales (seismic data, DInSAR data, extensometers, levelling, seismic surveys) in order to understand the behaviour of this fault in the complex dynamics of the eastern flank of the volcano. Furthermore, we analysed, in detail, ground deformation and seismicity occurring on TF during the best monitored episode (the last in February 2019), in response to the stress produced by the 24 December 2018 eruptive intrusion.

2. Materials and Method

Mt. Etna seismicity is monitored by the Istituto Nazionale di Geofisica e Vulcanologia—Osservatorio Etneo—Sezione di Catania (INGV-OE) permanent seismic network, which currently consists of about 30 stations deployed around the volcano. The geometry of the seismic network suffers from a nonoptimal coverage in the TF area, located in a peripheral and highly populated area of the volcano. From a ground deformation point

of view, since 2005, the TF has been monitored by two continuous extensometer stations. Seismic surveys have recently been carried out to investigate the structure and geometry of the TF. In particular, three MASW (multichannel analysis of surface waves) surveys and 41 ambient noise samplings were performed, divided between three alignments crossing the TF (Figures 1 and 2(c1–c3)).

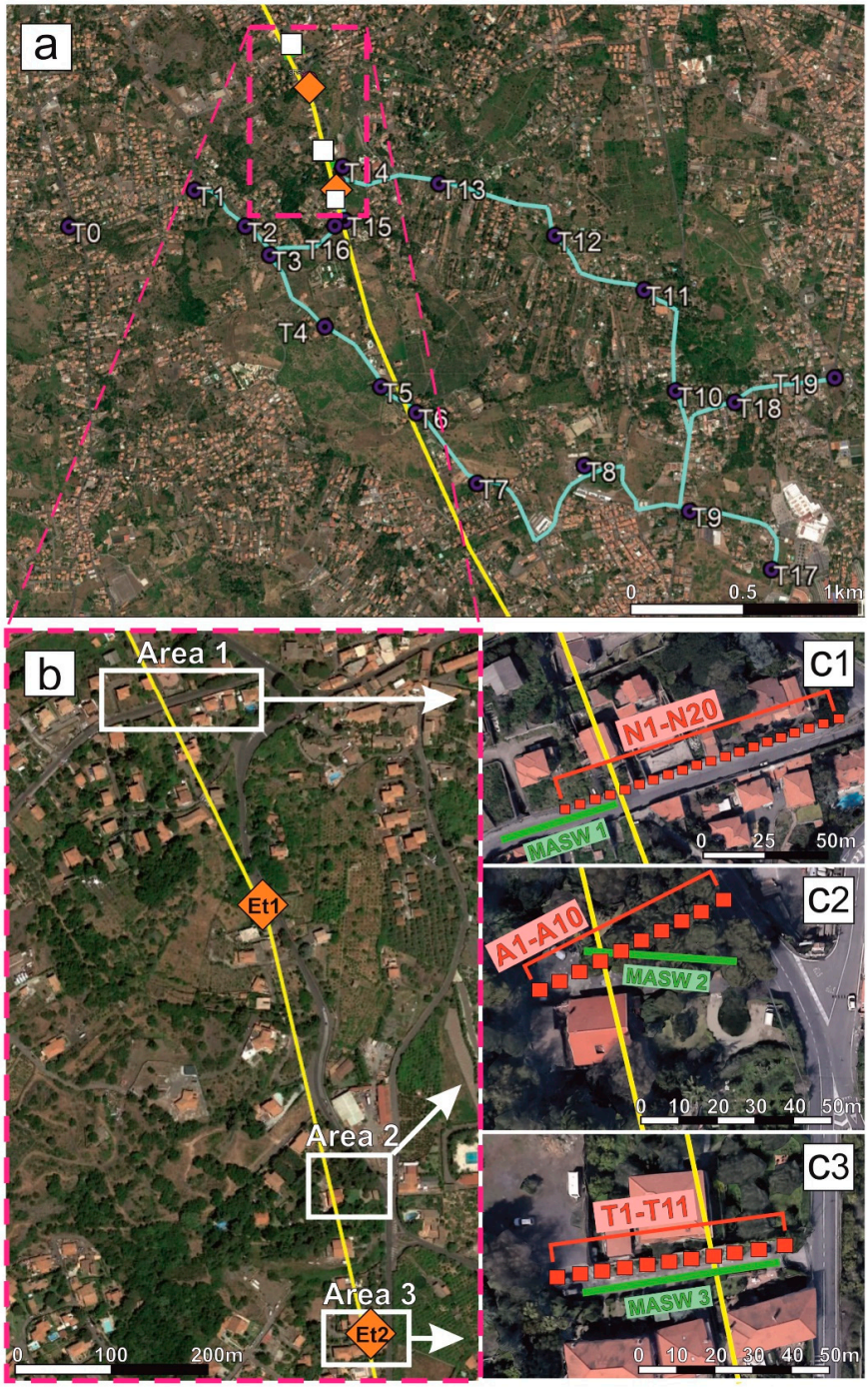

Figure 2. (**a**) Map of the levelling route (sky-blue line) across the Trecastagni Fault (TF). Blue circles indicate the levelling benchmarks; orange diamonds indicate the position of the extensometers. White squares indicate the location of seismic surveys. (**b**) Yellow line indicates the TF, and the extensometers are shown by orange diamonds (Et1, Et2). White rectangles (Area 1, Area 2 and Area 3) indicate the position of the geophysical surveys in the three different areas. (**c1–c3**) Red squares show the location of the sampling points of the noise, while the alignments of the MASW surveys are shown in green.

Furthermore, discrete ground deformation techniques such as In-SAR and levelling techniques are used to characterize the TF behaviour on a larger scale [8].

2.1. Seismic Network

During the last 40 years, the permanent seismic network located on Mt. Etna has undergone various configurations in its geometry, the number of stations and instrumental characteristics. In the late 1970s, a short-period seismic network, comprising five to nine stations, was managed by the University of Catania [37–39]. Since 1989, the network was run first by the Istituto Internazionale di Vulcanologia (IIV-CNR; 13 stations), then in 1999 by the Progetto Poseidon (44 stations), and successively, starting from 2001, the INGV-OE network has undergone, in about 20 years, various configurations (Figure 1). In fact, from 2005, the technology of several stations was upgraded from analogic short period 1-component to digital broad-band 3-component, and, at present, the INGV-OE permanent seismic network consists of about 30 stations (Figure 1).

2.2. Extensometers

From a ground deformation viewpoint, currently, in the study area, there are two continuous extensometer stations (Et1 and Et2 in Figure 2a,b) managed by the INGV-OE (Mod Sisgeo D241A20) and equipped with compact data-loggers programmed for 48 data/day sampling (Figure 2; [31,40]). The instruments measure the relative displacements perpendicular to the fracture; Et1 was installed in May 2005 on a fractured concrete structure, and Et2, at the end of 2007 on the ground inside a trench 8 metres long and 30 cm deep. The measurements with extensometers carried out across the TF in the period 2005–2009 showed that the fault is characterized by an average continuous extension rate of about 2–3 mm/year [8]. However, when seismic activity occurs along TF (e.g., on 9 February 2019, Ml = 2.9), an acceleration of the extension was measured with variations up to 12 mm in just a few days [31,41].

2.3. Levelling

In order to measure the vertical displacement of the Trecastagni Fault with the greatest detail and best accuracy, a levelling network was set up in November 2009 over the area affected by the maximum vertical slip [28,42,43] and measured five times (the last in September 2021). The network (Figure 2a) consists of a main loop (about 6 km long), crossing the fault twice on the northern and southern sides and allowing for the verification of the closure errors, and three open lines made to extend the areal coverage both on the hangingwall and footwall. Three branches start off from the main loop: one extending westwards (from T3 to T0) towards the stable part (footwall), and two extending eastwards (from T10 to T19) and south-eastwards (from T9 to T17) towards the area showing the maximum subsidence rate (hangingwall). The entire levelling network is 9 km long, distributed along the roads close to the geological structure, and consists of 20 benchmarks [8]. Surveys were carried out with an electronic Leica DNA03 level, an optical level Wild NA2 equipped with parallel-plate micrometre (resolution of 0.01 mm) and invar rods; instruments were calibrated every day before the measurements. Maximum accepted discrepancy (in mm) between the height differences measured during forwards and backwards paths is $\pm 2.5\ (L)^{1/2}$, where L (in km) is the length of levelling section; the maximum error (in mm) allowed for the closure of the loop is $\pm 2.0\ (C)^{1/2}$, and C (in km) is the length of the circuit [8,44,45].

2.4. DInSAR Analysis

DInSAR data are acquired from the Sentinel-1A/1B satellite operating under the Copernicus program of the European Space Agency (ESA) available from https://scihub.copernicus.eu/dhus/ (accessed on 30 March 2019). The processed images were acquired in TopSAR (Terrain Observation with Progressive Scans SAR) Interferometric Wide (IW) mode (VV polarisation; vertical transmit and receive polarisation), along the descending orbit.

The Sentinel-1A data were processed by GAMMA software [46], using a spectral diversity method, and a procedure able to co-register the image pairs with extremely high precision (<0.01 pixel). The interferograms were produced by applying a two-pass DInSAR processing and multilooking pixels (5 × 1 in range and in azimuth) in order to maintain the full ground resolution (11 m × 13 m). The topographic phase was removed from the interferograms by using the SRTM V4 digital elevation model (DEM) generated by Shuttle Radar Topography Mission (SRTM) with three arc-second ground resolution (about 90 m) [47].

2.5. Seismic Surveys

2.5.1. MASW Surveys

MASW is an active seismic technique based on the analysis of surface waves (Rayleigh waves), which are propagated with a velocity related to the rigidness of the subsoil portion affected by the wave propagation [48]. The waves, generated by an energization source, are recorded through a geophone alignment arranged on the ground surface, in order to define the 1D shear waves (V_s) velocity profile.

In this study, three MASW surveys (Figures 1 and 2(c1–c3)) were carried out using a digital multichannel array equipped with vertical geophones with a natural frequency of 4.5 Hz. The number of geophones used are respectively 16 for MASW1, 17 for MASW 2 and 23 for MASW3; they were arranged on the ground with an interdistance of 3 m.

The energization system used comprises an 8 kg sledgehammer and an iron base. In order to increase the energy content and improve the signal-to-noise ratio for each survey, five shots were carried out at 6 m from the beginning and the end of the alignments (stacking method). Each signal was acquired for 3 s, using a sampling frequency of 512 Hz.

The acquired data were processed using the SeisImager software. In this software, the phase velocity is calculated starting with setting parameter "phase velocity end" to the maximum speed expected for the site. Subsequently, parameters for selecting the maximum amplitudes, which define the dispersion curve on the phase velocity–frequency graph, are set. The experimental dispersion curve was obtained using the Pickwin application (Figure 3a), performing the picking of the dispersion curve on the maxima of the spectrum absolute value, considering the dispersion curve to consist mainly of a fundamental mode. The initial V_s-depth model is calculated from the one-third wavelength approximation. An inversion process (least square method) implemented on WaveEq (SeisImager software, v. 3.0, Geometrics, San Jose, CA, USA) was used in order to define 1D V_s-depth profiles (Figure 3b). In this process, the initial model was modified repeatedly in order to obtain the best fit between the model and the observed data.

For each MASW, the phase velocity–frequency spectra were calculated for both forwards and reverse shot positions, and the related dispersion curves were obtained. Between the two dispersion curves obtained for all the three MASW surveys, we chose to use the dispersion curve related to the forwards shot that presented the clearest results with acceptable RMS values (Figure 3).

2.5.2. HVSR Surveys

The horizontal-to-vertical spectral ratio (HVSR) [49,50] is a passive seismic method based on the sampling of ambient seismic noise [51]. This technique uses the recording of ground motion in the three spatial components to estimate the resonance frequency of the site by computing the H/V spectral ratio between the average of horizontal components on the vertical one.

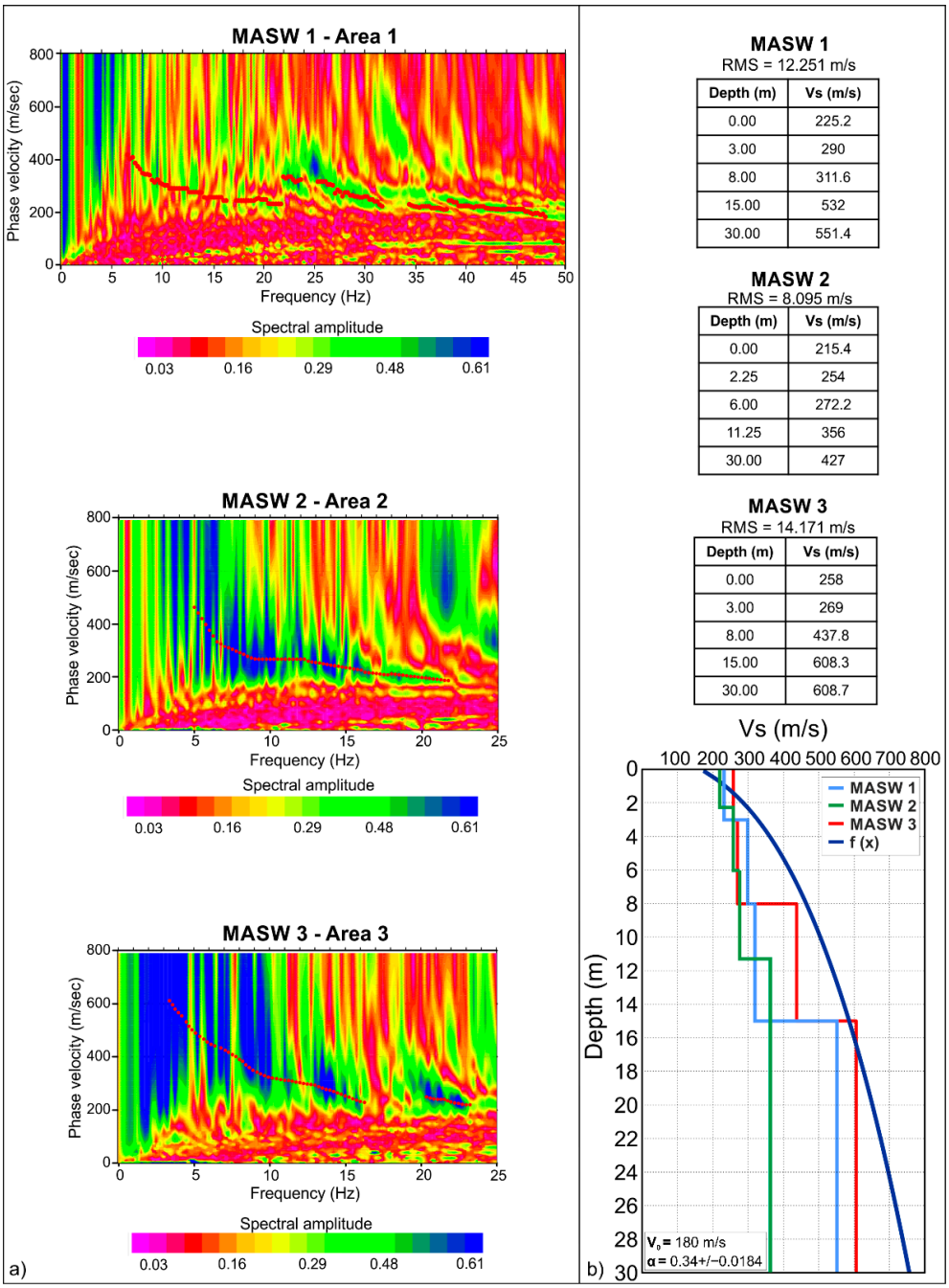

Figure 3. (**a**) Dispersion curves obtained from the three MASW surveys; (**b**) 1D velocity–depth profiles, where the blue curve represents the function (2) that has the minimum misfit with the data of the 1D velocity depth profiles obtained from the MASW surveys.

The ambient seismic samplings were carried out using five 3-component velocimeters. The measurements were performed along three different profiles, crossing the Trecastagni Fault (Figure 2(c1–c3)), with an interdistance of 5 m.

The first two alignments, oriented approximately SW–NE, consisted of 20 and 10 ambient noise measurements, respectively, while the third alignment, performed with 11 sampling points, was oriented about WSW–ENE.

All recordings were acquired for 20 min with a sampling frequency of 128 Hz, and the instruments were arranged with the N–S component parallel to the north direction.

Seismic ambient noise measurements were processed, with the HVSR method, using Grilla software. All records were elaborated in the frequency range 0–64 Hz (half of the

sampling rate), dividing the traces into 20 s long windows. In addition, to each window was applied a 10% smoothing with a triangular window type. In order to obtain the H/V spectrum, the average of the H/V spectral ratios obtained from each window were calculated. After that, the spectral ratios were determined by rotating the N–S and E–W components by 10° increments from 0° (North) to 180° (South). This method is effective to point out directional effects, if any, linked with the fault presence.

The H/V spectra were analysed with the corresponding single components Fourier spectra to identify the presence of peaks attributable to stratigraphic variations and distinguish them from those related to anthropic noise.

Many researchers have used the HVSR technique to obtain information on subsoil stratigraphy [52–56]. HVSR data can be integrated with the 1D V_s-depth velocity model in order to obtain a graphic reconstruction of the subsoil seismostratigraphic features, known as impedance contrast section [57–65]. The impedance contrast sections show the H/V amplitude distribution in the subsurface. The presence of a discontinuity between lithotypes with different physical and mechanical properties causes an impedance contrast in the subsurface. Consequently, the identification of impedance contrasts allows for obtaining information on the geological and structural characteristics of the subsoil.

Even if the relationship between the H/V amplitude value and the degree of impedance contrast is not linear, the higher the impedance contrast, the greater the amplitude of the spectral peak.

Considering a two-layer system, characterized by different values of velocity (V_1, V_2) and density (ρ1, ρ2), if the resonance frequency (f) and the shear wave velocity (V_s) are known, it is possible to obtain the thickness of the resonant layer (H), according to this relationship:

$$f = V_s/4H \quad (1)$$

Generally, the shear waves velocity increases with depth, as a result of increased lithostatic loading. This relationship can be expressed by the following function [66]:

$$V_s\,(z) = V_0\,(1 + z)^{\alpha} \quad (2)$$

where:
V_s = shear wave velocity;
V_0 = shallow shear wave velocity;
z = depth;
α = proportionality coefficient depth-velocity.

This equation was used to fit the 1D V_s-depth profiles obtained from the MASW surveys. The V_0 = 180 m/s and α = 0.34 +/− 0.0184 values for which the minimum misfit exists between the function and the experimental profiles were obtained (Figure 3b).

The HV spectra frequency values were converted into depth values using V_0 and α parameters in the Ibs-von Seht and Wohlenberg formula [66]:

$$h = [(V_0\,(1 - \alpha)/4f - 1]^{(1/((1 - \alpha)))} - 1 \quad (3)$$

The impedance contrast sections were obtained by integrating, with the Kriging interpolation grid algorithm, the data relating to each sampling point acquired with regular interdistance.

3. Results

3.1. Seismic Survey Data

The 1D velocity profiles, related to the MASW surveys performed on Areas 1 and 2, display at shallow depth, ranging between 0 and 3 m, a shear wave velocity value of around 220 m/s. Below this layer, the shear wave velocity increases progressively with depth, reaching values of about 550 m/s at a depth of 15 m for the MASW 1 and 427 m/s at a depth of 11 m for the MASW 2 (Figure 3b). The RMSs associated with the models

are 12.251 m/s and 8.095 m/s, respectively. The third velocity profile (RMS = 14.171 m/s) related to Area 3 exhibits slightly higher shear wave velocity values: the first layer is characterized by shear wave values of about 260 m/s, gradually reaching values of 608 m/s at depth (Figure 3b). The three profiles have a similar trend with the difference that the third profile shows higher velocity values. (Figure 3b).

Based on the geological features of the investigated areas [67] and on the few outcrops present in the studied sites, it is possible to associate the first layer of each profile, characterized by low velocity values, as attributable to the presence of loose rock, such as pyroclastic products, while the velocity increase with the depth would point to the presence of lava rocks with different fracturing degrees.

The H/V spectra obtained by the passive seismic surveys performed in the three investigated areas reveal H/V amplitude values lower than 1 at high frequencies, probably related to the effects of the flooring above which the surveys were carried out. The spectra, related to the acquisitions performed in Areas 1 and 2 (Figure 4a), highlight a significant "broadband" peak that can be associated with a stratigraphic transition. The shape of the H/V spectra obtained in the third area is different (Figure 4a): the spectral peak appears more pronounced, probably due to the presence in the subsurface of a sharper impedance contrast.

The polar diagrams (Figure 4b) clearly exhibit an evident directional effect linked with the fault presence. The directional effect, related to the spectral peak, is about WNW–ESE-oriented and forms an angle of 30–40° with the fault's strike.

Comparing all the HVSR spectra for the same alignment (Figure 5a–c), it can be seen that the H/V peak is at a lower frequency for measurements located east of the tectonic structure than for samplings to the west, suggesting that a more massive layer deepens from the west to the east.

In order to enhance this effect, integrating the data from the active and passive seismic surveys, impedance contrast sections were reconstructed for the three investigated areas (Figure 5a–c).

Section 1 reveals at low depth a seismolayer characterised by low H/V amplitude values and variable thickness from about 10 m up to 20 m. This layer can be associated with the presence of pyroclastic or fill material (Figure 5a).

Below this layer, a strong impedance contrast is observed, distinguished by high H/V amplitude values (>2.5), caused by the presence of a change in the subsoil characteristics probably associable with the presence of lava rocks with different fracturing degree.

The rocks with higher contrast, at about 20 m from the start of the profile, where the Trecastagni Fault crosses the section, seem to be displaced. It is possible to estimate a fault displacement of about 10–15 m. (Figure 5a)

Similar to what is reported in Sections 1–3 also present a first layer identified by low H/V amplitude values, less than 1.4, with a thickness around 10–20 m (Figure 5b,c). Even in this case, these layers can be associated with the presence of pyroclastic or fill material. At greater depths, it is possible to observe an impedance contrast (H/V amplitude value > 2.5), probably related to the presence, below the pyroclastic layer, of lava rocks.

In this case, the effect of dislocation linked to the presence of the tectonic structure is visible at about 20 m and 35 m, respectively, from the beginning of the sections, and the estimated displacement is equal to about 15 m.

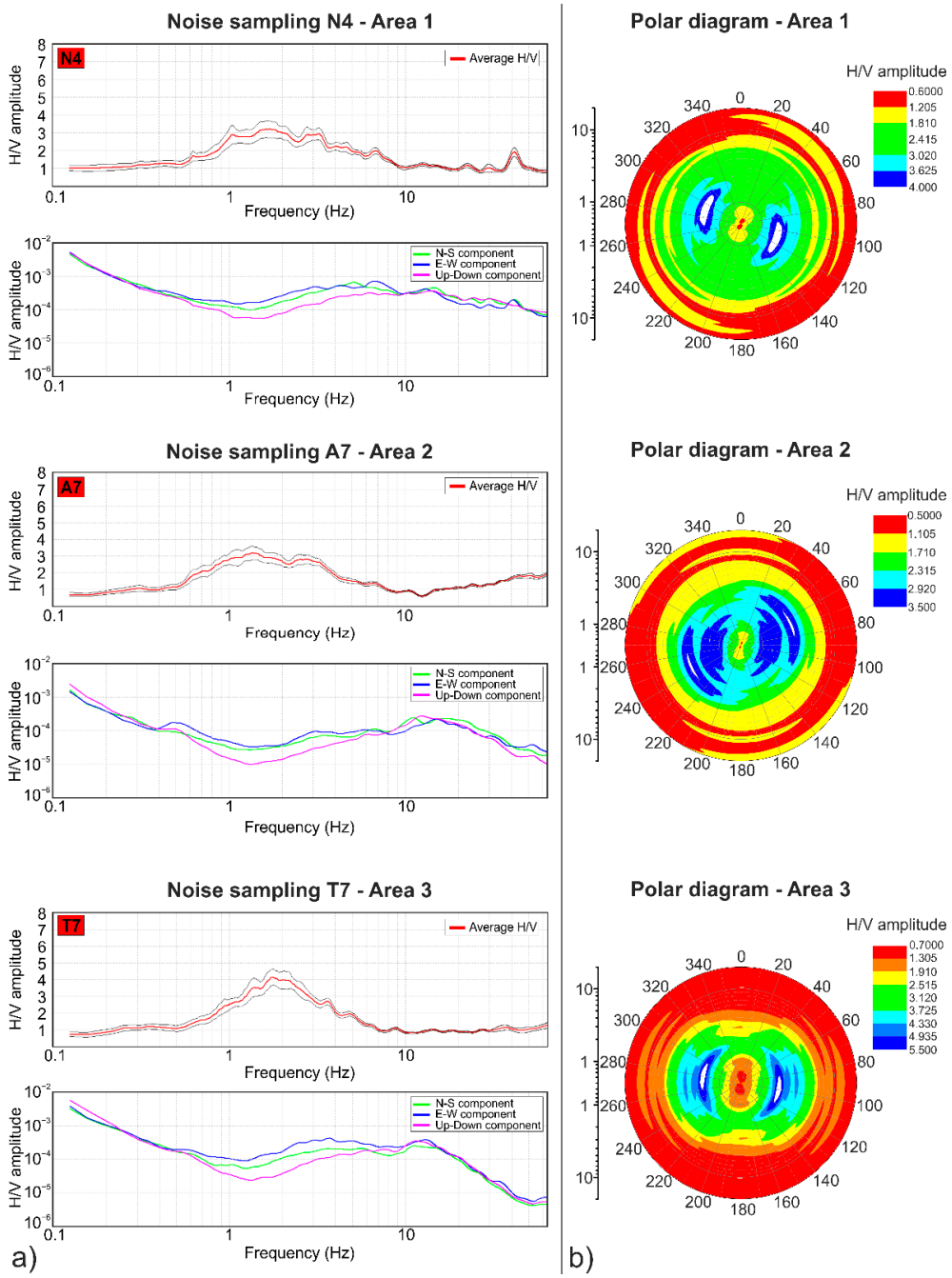

Figure 4. (**a**) Examples of HVSR spectra (**up**) and spectral amplitudes of single components (**down**) and polar diagrams (**b**) relating to seismic ambient noise records.

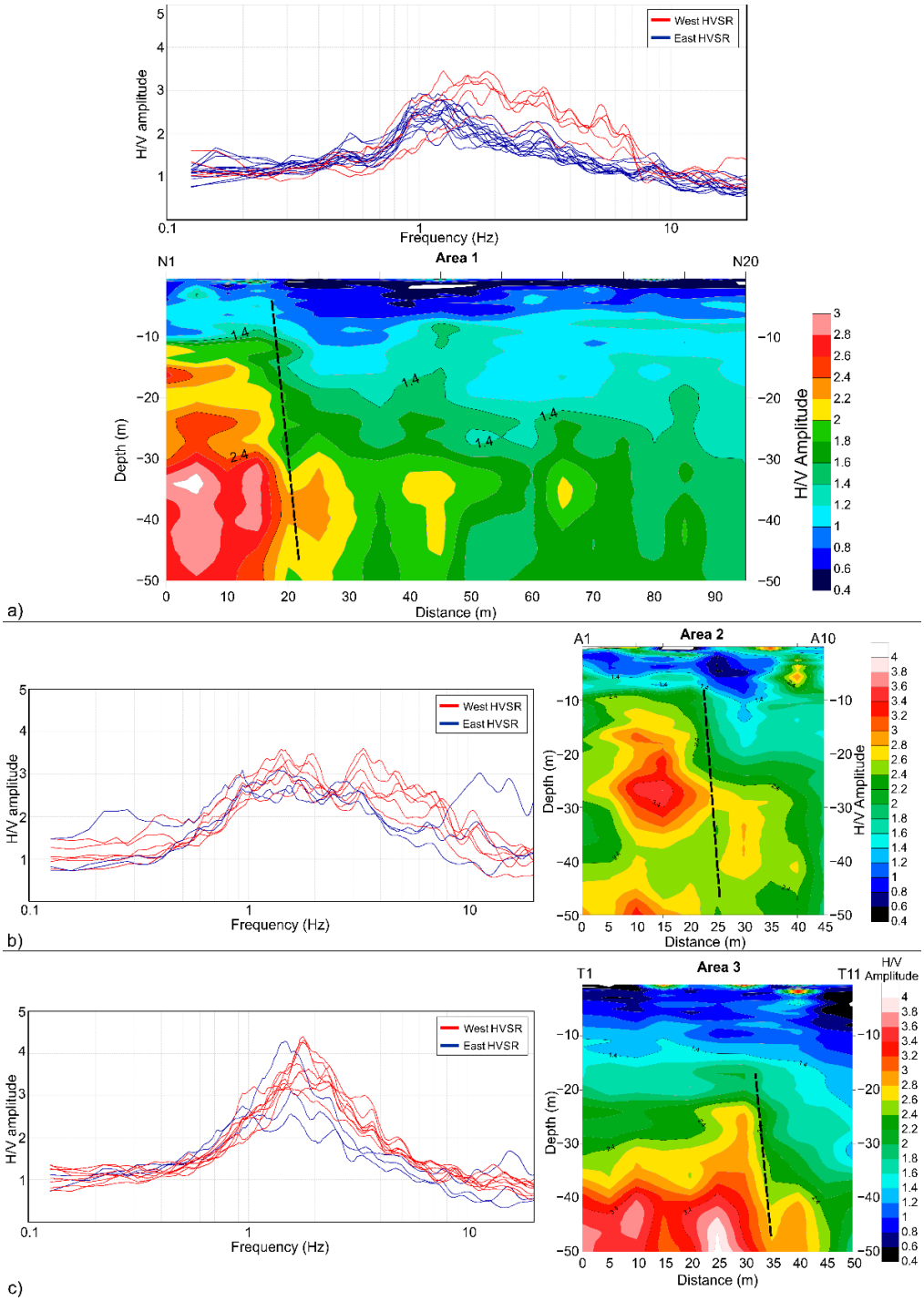

Figure 5. HVSR spectra (the red and blue spectra are related to the measurements sampled at the west and east side of the fault, respectively) and related impedance contrast sections (the dotted line represents the location of TF) for: (**a**) Area 1, (**b**) Area 2 and (**c**) Area 3.

3.2. Seismological Framework

Evident co-seismic surface faulting occurred along the fault scarp of TF in September 1980 and in November 1988 [68]. Hollows appeared in agricultural land, and fractures in buildings, boundary walls and the road 8/III were observed after the local shocks on 16 September (Md = 2.9, Io = VI) and 28 September (Md = 3.1, Io = VI) 1980 and also after the 21 November 1988 earthquake (Md = 3.4, Io = VI) [68]. Other similar episodes on 21 December 1634 (Io = VI, VII), 26 May 1903 (Io = V, VI), 20 July 1917 (Io = V, VI),

17 February 1955 (Io = V, VI), 7 November 1984 (Io = V, VI; Md = 3.5) and 31 October 2005 (Io = VI; Md = 3.6 and 3.5) have been reconstructed by historical research [69]. In recent years, several shallow earthquakes of very low magnitude (not analytically localizable) occurring in October 2009, October 2010 and February 2019 [26,33] were felt by the local residents near the epicentral area.

In order to provide a detailed seismic picture of this tectonic structure, we considered the instrumental seismic activity, in the period between 1980 and April 2021, within an area which includes the surface evidence of the TF. Our study area, located in the lower-middle southern sector of the volcanic edifice, has a rectangular shape with a predominantly NW–SE orientation which extends for about 1200 m both east and west from the TF (Figure 6a). To this end, the data recorded by various seismological observatories over the last forty years or so and reported in various instrumental catalogues were collected. In particular, we used two seismic catalogues: (i) the first (C2.5) was compiled, merging the earthquakes recorded in the time interval 1980–April 2021 and available in the databases of the University of Catania (UNI-CT; [70]), Istituto Internazionale di Vulcanologia (IIV-CNR; [39]) with that of INGV-OE [71–76], using the earthquakes with a magnitude greater than or equal to 2.5; (ii) the second (CALL) consisted of all earthquakes located by the INGV-OE permanent seismic network, with a magnitude greater than 1.6, in the period 2000–April 2021. For the C2.5 catalogue, we chose to use the threshold of magnitude 2.5 to unify the three catalogues, which, over time, have been influenced by the different geometry of the networks and their instrumental characteristics. In particular, before the year 2000, the value of magnitude 2.5 represents a reference value as minimum magnitude ([39]).

A statistical approach to the CALL catalogue in order to calculate the magnitude of completeness (Mc) was applied. We only considered the CALL catalogue because the C2.5 one includes few events, all with magnitudes between 2.5 and 3.5, without the contribution of low-medium–energy earthquakes. Mc is theoretically defined as the lowest magnitude at which 100% of the earthquakes in a space–time volume is detected [77,78]. We used ZMAP software, which allows the estimation of both Mc and the parameters of the Gutenberg–Richter relationship [79]. Applying the maximum curvature method [78], an Mc value equal to 1.6, with uncertainty of 0.13, was obtained (Figure 6c).

The C2.5 catalogue comprises 51 earthquakes with maximum local magnitude (ML) equal to 3.5, while the CALL has 120 earthquakes with ML ranging between 1.6 and 3.8.

Therefore, the catalogue CALL comprises 27 earthquakes belonging also to C2.5.

The average values of epicentral and hypocentral errors of locations are 0.6 km and 0.8 km, respectively.

In order to evaluate the temporal distribution of seismicity, all earthquakes were used to compute the daily rate occurrence and the related seismic strain release. The seismic energy (E) in Erg is computed using the relationship $\log E = 9.9 + 1.9M - 0.024M^2$ [80].

In general, the C2.5 catalogue shows some periods characterised by intense seismicity releases interspersed with long periods of very low activity (Figure 6a). In particular, three periods of strong seismic activity were observed between October 1983 and September 1985 and in July 2002 and October 2005. On the contrary, during the periods 1986–early 1998 and late 2005–2020, very low seismic activity was observed (Figure 6a,b). It is worth highlighting that the seismicity of the 2000–2020 period is comparable to that of the first twenty years. For the CALL catalogue, as reported in Figure 6b, after the last major release of 2005, an almost constant energy release was observed with weak seismicity episodes (September 2009, July 2014 and February 2019).

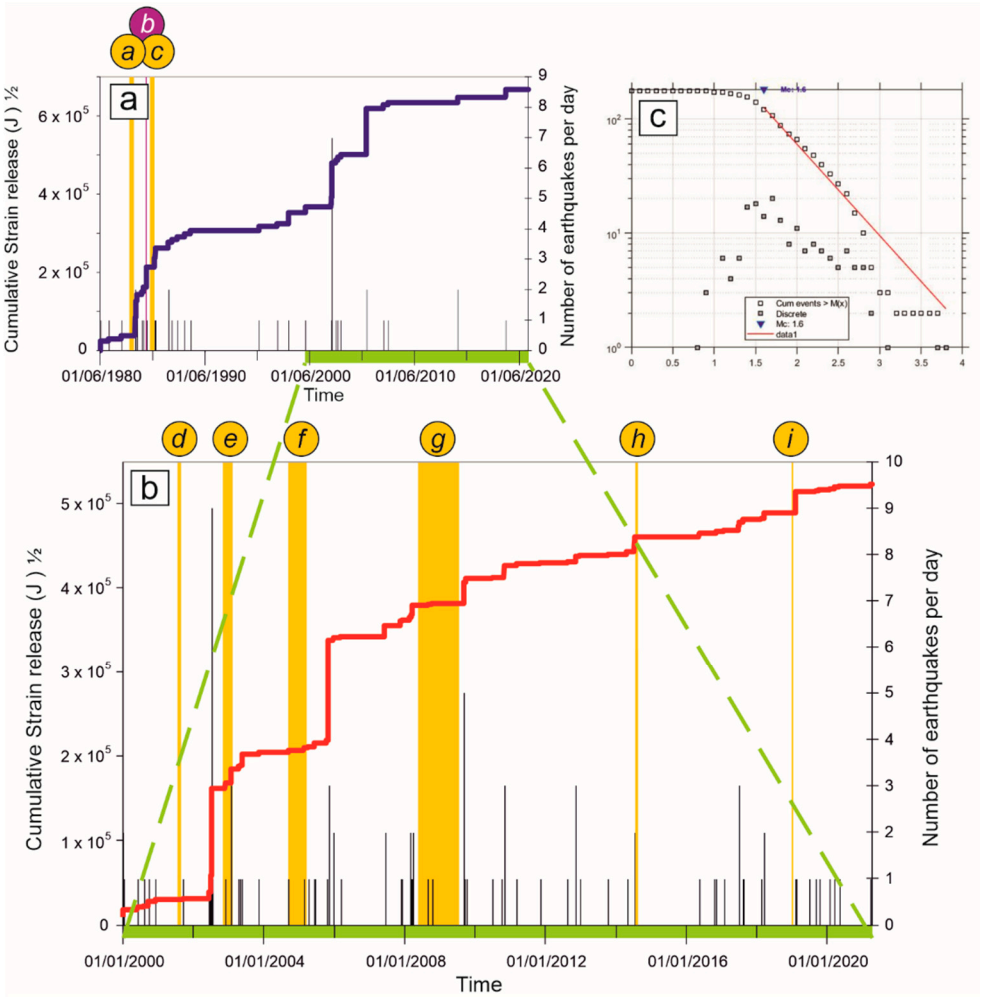

Figure 6. Daily earthquake occurrence and related cumulated strain release for (**a**) C2.5 catalogue and (**b**) CALL catalogue. The periods marked in yellow indicate the main flank eruptions. a: 1983 eruption; b: 1984 Fleri swarm; c: 1985 eruption; d: 2001 eruption; e: 2002–2003 eruption; f: 2004–2005 eruption; g: 2008–2009 eruption; h: South East Crater 2014 activity; i: February 2019 seismicity. (**c**) Magnitude–frequency distribution of earthquakes during the period 2000–2021 for CALL catalogue. Solid triangles represent the number of earthquakes for magnitude class; empty squares indicate the cumulative number of earthquakes greater than or equal to the relative magnitude class. The dashed black line represents the Gutenberg–Richter (G–R) relationship. Mc is the magnitude of completeness.

The earthquakes were located using the Hypoellipse algorithm [81] and Hypo71 [82] for the C2.5 catalogue and CALL catalogues, respectively, and the 1D crustal velocity model proposed for Mt. Etna area by Hirn et al., 1991 [83], and subsequently modified by Patanè et al., 1994 [84], for both catalogues.

Figure 7a shows the epicentral map of the earthquakes constituting the two catalogues (C2.5 and CALL) in the period 1980–April 2021. Most of the seismicity is located in the north-western portion, while the central and southern sectors are characterised by low seismic activity (Figure 7a). In particular, the north-western sector is mainly characterized by shallow earthquakes, while in the southern sector the deeper seismicity is predominant. This evidence is also confirmed by the cross-section shown in Figure 7b. Again, in the north-western sector of the study area, the most energetic earthquakes occurred in October 2005 (Md = 3.6 and 3.5).

Table 1. Earthquakes occurring in February 2019 with main hypocentral location parameters.

Number Event	DD/MO/YR	Origin Time	Latitude	Longitude	Depth (km)	Ml	No	GAP (°)	RMS (s)	ERH (km)	ERZ (km)	D (km)
1	06/02/2019	23:38:04.91	37.591	15.085	0.49	2.5	29	103	0.30	0.30	0.50	3.9
2	09/02/2019	06:02:19.05	37.576	15.094	2.63	2.9	24	88	0.25	0.20	0.20	2.2
3	10/02/2019	04:00:17.00	37.599	15.073	1.28	2.4	18	140	0.16	0.40	0.90	5.3

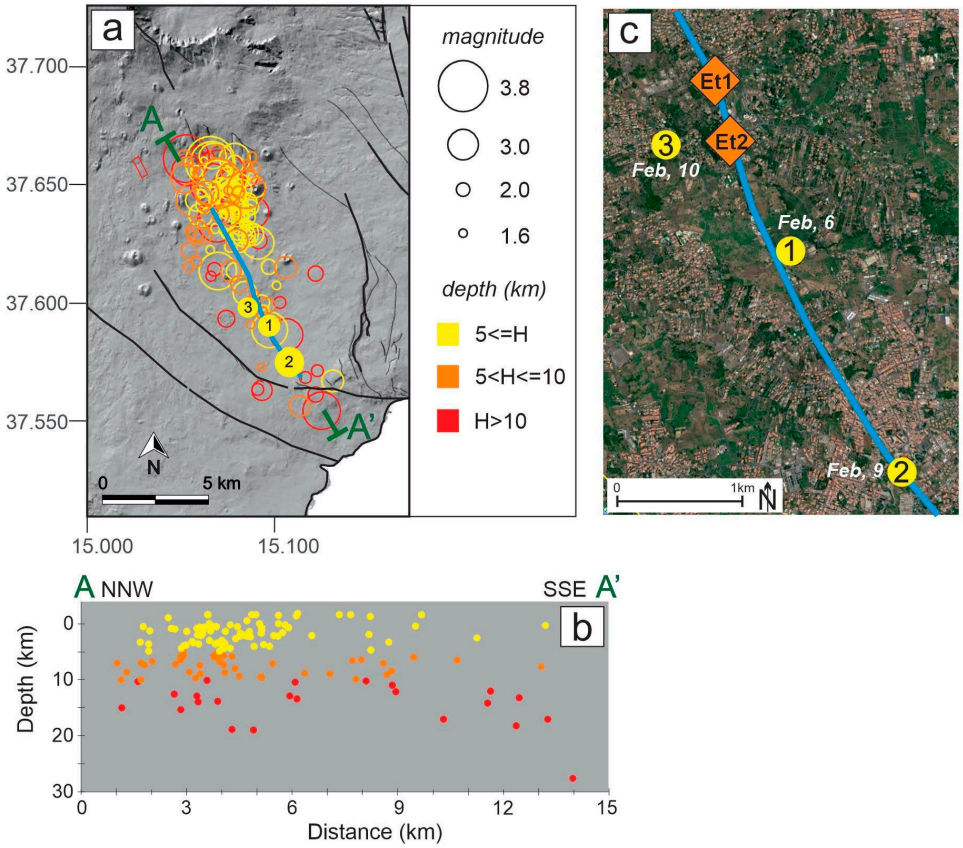

Figure 7. (**a**) Epicentral map of earthquakes belonging to C2.5 and CALL catalogues in the period 1980–April 2021. Coloured circles and their size indicate range depth and magnitude values, respectively; (**b**) cross-section along TF in the NNW–SSE direction; (**c**) epicentral map of February 2019 seismicity (numbered yellow circles; see Table 1) and location of extensometer Et1, Et2 (red diamond); blue line: Trecastagni Fault.

As regards the hypocentral depths, the different network geometry and therefore the dissimilar detection capacity did not allow us to make a comparison for the entire period, so we focused on the last twenty years (2000–April 2021; CALL catalogue). The depth distribution of the earthquakes in the CALL catalogue highlights that the seismic release is mainly characterised both by isolated shocks and medium energy swarms that occur mainly within the first 10 km of depth (Figure 8a).

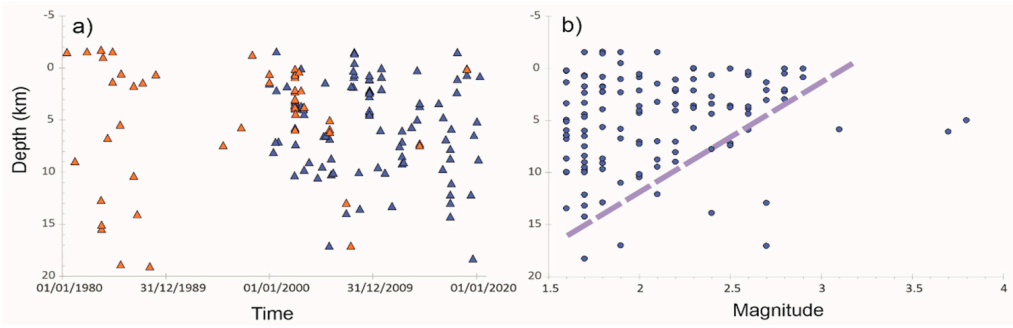

Figure 8. (**a**) Diagram showing time vs. depth for C2.5 catalogue (red triangles) and for CALL catalogue (blue triangles); (**b**) diagram showing magnitude vs. depth (see text for details).

Furthermore, it is worth pointing out that the strongest earthquakes occur only within the first 5 km of depth and that over 10 km only low-magnitude earthquakes occur. Therefore, it seems that, with the exception of the three most energetic earthquakes, the hypocentral depths and the magnitudes follow an inverse proportionality ratio; in fact, as the depths decrease, the frequency of occurrence of the most energetic events increases (Figure 8b).

Seismic Data Integration: The February 2019 Seismicity

Since the geometry of the INGV-OE seismic network is sparse in the southern sector of volcano, we added a station (SGR) managed by an agreement between the Dipartimento di Scienze Biologiche, Geologiche e Ambientali of the University of Catania and the Municipality of S. Gregorio di Catania. This station SGR, located in San Gregorio di Catania territory, near the Trecastagni Fault, is equipped with a short-period three-component seismometer (Figure 1). We focused on three earthquakes that occurred in the posteruption December 2018 phase. They occurred on 6 February 2019 (23:38 UTC Ml = 2.5), on 9 February (06:02 UTC, Ml = 2.9) and on 10 February (04:00 UTC, Ml = 2.4) and were felt by the local people living near the epicentral area (Figure 7b).

We collected the readings of the P and S phases recorded by the INGV-OE seismic network with those of the SGR station. These earthquakes were located using the Hypoellipse algorithm [81] and the 1D crustal velocity model [83] and subsequently modified by Patanè et al., 1994 [84]. This integration allowed us to improve the main hypocentral location parameters (GAP; RMS, ERH and ERZ), to decrease the distance of the nearest station to the epicentre and to better associate and constrain these earthquakes with the geometry and position of the TF (Figure 6b and Table 1). It is worth highlighting that the earthquake of 10 February (Ml = 2.4) was very close to the position of the Et2 extensometer (Figure 7b).

3.3. Extensometer Data

Data collected over 16 years of recording (2005–2021) highlighted how TF was affected by an opening of ca 35 mm (about 2 mm/year) that Et1 records as a continuous increase, while Et2 is characterized more by a step-like behaviour (Figure 9).

Three increase episodes were recorded in 2009, 2016 and 2019, which indicated an acceleration of the TF dynamic linked with the Mt. Etna flank seawards movements [28].

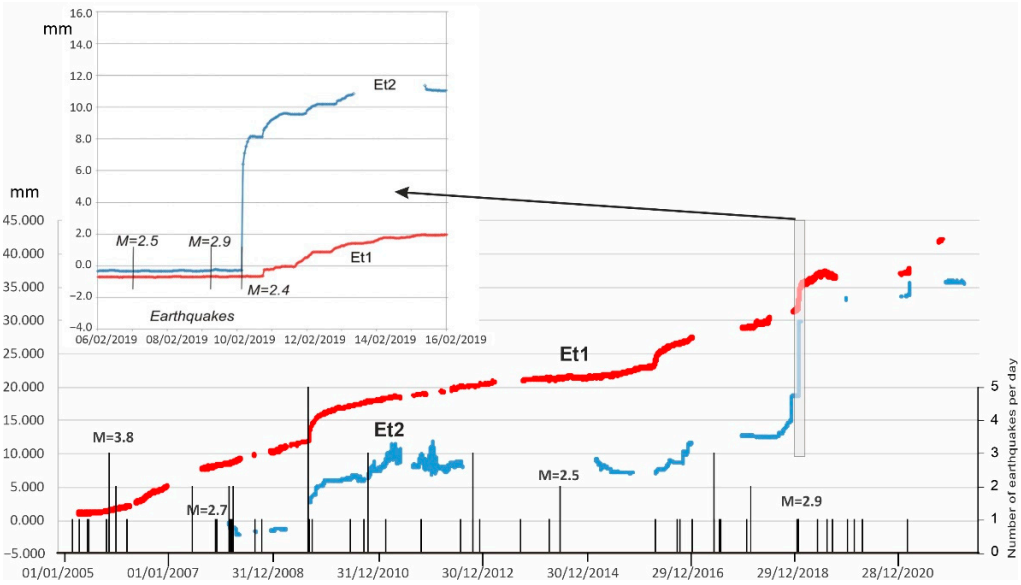

Figure 9. Extensometers data recorded at Et1 and Et2 stations (2005–2021). Daily earthquake occurrence from Figure 6. In the inset, the signals recorded during 6–16 February 2019 and timing of the earthquakes.

The 10–15 February 2019 event is certainly the most important episode, and extensometers recorded the fault dynamic immediately after the last of the three earthquakes recorded. Data indicated a sharp increase at Et2 in correspondence of the 10 February at 04:00 GMT event, accumulating with an opening of about 8 mm in the first few hours and 11 mm in five days. Et1 station showed less variation (about 2.5 mm) and a delay in its activation of about 14 h.

Fault activation took place progressively through seismic releases between 6 and 10 February and subsequently in the period between 10 and 15 February without seismic activity (Figure 9).

3.4. Levelling

Levelling measurements were carried out in November 2009, March 2010, March 2011, May 2019 and September 2021.

The reference benchmark used to compute the height variations was the benchmark T1, which lies on the western side (footwall) of the fault, at about 0.5 km away from it; the position of this benchmark was chosen from PS maps [28], in a stable area that was unequivocally outside the subsiding block bordered by the fault.

By comparing results of the November 2009 survey with those of the successive ones, the slip related to the Trecastagni Fault can be detected and followed in time. In this 12-year comparison, a clear jump of about 7–8 cm affected stations across the fault both in southern and northern sides (Figure 10). Indeed, while all benchmarks lying on the western side of the fault recorded very low variation in their vertical positions with respect to T1 benchmark from November 2009 to September 2021, those lying just east of the structure were affected by a subsidence of several centimetres that gradually decreased towards the east, away from the fault. Fault traces intersected the levelling route between benchmarks T5–T6 on the southern side and between the benchmarks T15–T16 on the northern one (Figure 2a).

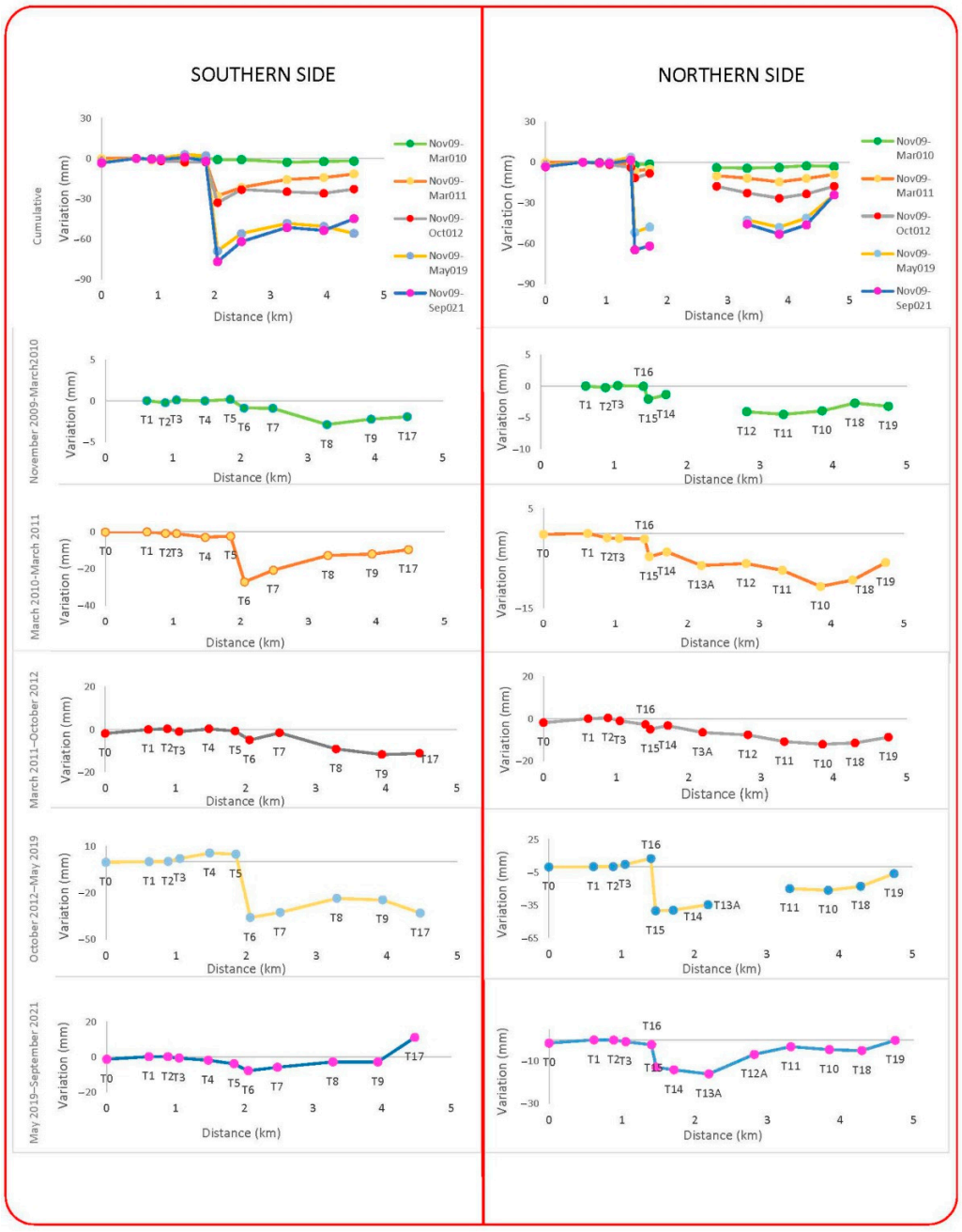

Figure 10. Vertical displacements measured by the levelling surveys on the southern and northern sides of the network. In the first row, the cumulative effects of the dislocation are plotted for each side by comparing each survey with the first one of 2009. In the following rows, each survey is compared with the previous one to show each subsequent period independently for evidencing the changes of behaviour of the fault in time for each side of the levelling route across the fault.

Concerning the time series of the benchmarks crossing the fault (T5–T6 in southern side and T15–T16 in northern side Figure 11), large variations were recorded in the period 2012–2019. Due to the longer time period, vertical displacements are overall more significant than the other comparison but fall within the average rate; however, a comparison with extensometer data suggests that a significant part of these changes is attributable to the February 2019 event. Conversely, the displacement measured from 2010 to 2011 on the southern side reveals a higher rate of deformation.

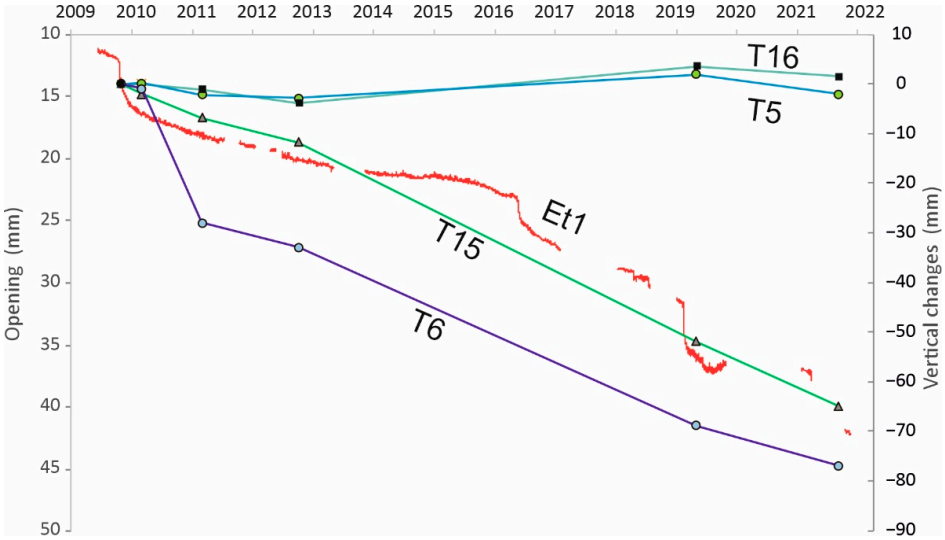

Figure 11. Time series of vertical changes at the benchmarks crossing the TF (T5–T6 in southern side and T15–T16 in northern side) compared with 2009–2021 extensometer data (ET1).

3.5. Most Recent Deformation Transient Detected by 2019 DInSAR Data

We performed a DInSAR analysis of C-band Sentinel-1A/1B data referring to available images acquired between 28 December 2018 and 14 February 2019.

We chose to analyse a longer time span with respect to the 2019 Trecastagni seismic events in order to provide a more complete picture of ground deformation affecting the whole volcano and its time–space evolution. In particular, we analysed the 1-month ground deformation starting from 28 December 2018, immediately after the December 2018 dyke intrusion and the 26 December Fiandaca earthquake, until 27 January.

The ascending/descending interferograms (Figure 12) map the movements occurring on the whole volcano, along the Pernicana fault to the north, along the Fiandaca fault to the south-east and along the Calcerana fault to the south-west. The comparison of the ascending and descending interferograms evidences a general asymmetric deformation pattern, suggesting a stronger horizontal component of the ground deformation, compatible with a radial ground deformation pattern probably due to an "adjustment" of the volcanic edifice after the huge deformation during the December 2018 dyke intrusion and the Fiandaca earthquake. We highlight here that no ground deformation was detected along the southern structures of the volcano and, in particular, no ground deformation was detected along the Trecastagni Fault during the investigated period.

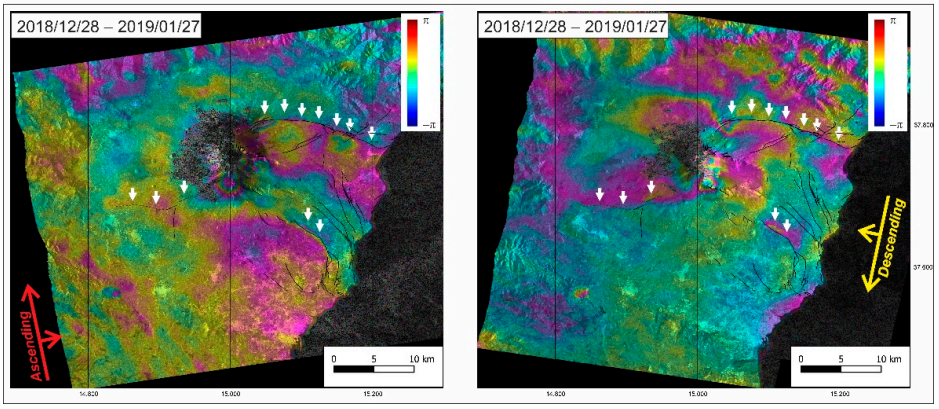

Figure 12. Ascending/descending interferogram from 28 December 2018 to 27 January 2019. White arrows indicate the fault lines bounding the ground deformation features observed.

The successive analyses focused on the spatial/temporal ground deformation evolution on Mt. Etna's southern flank and, in particular, on the ground deformation occurring along the Trecastagni Fault. We selected two time periods conforming with seismic events during the first February decade. During the first period, from 27 January to 8 February, a ground deformation of about 1 cm was visible along the Trecastagni Fault, localised very close to the ML 2.5 seismic event on 6 February; furthermore, a wider deformation was evident along the S. Gregorio-Acitrezza fault (white arrows in Figure 13), occurring in this short period. In the second 6-day period (from 8 to 14 February), the interferograms detected ground deformation localised northwards along the fault, with respect to the previous period, in accordance with the hypocentral location of the ML 2.4 event on 10 February, but no deformation was associable to the ML 2.9 seismic event. In Figure 13, we report the cumulative (18 days) ground deformation image by the DInSAR data.

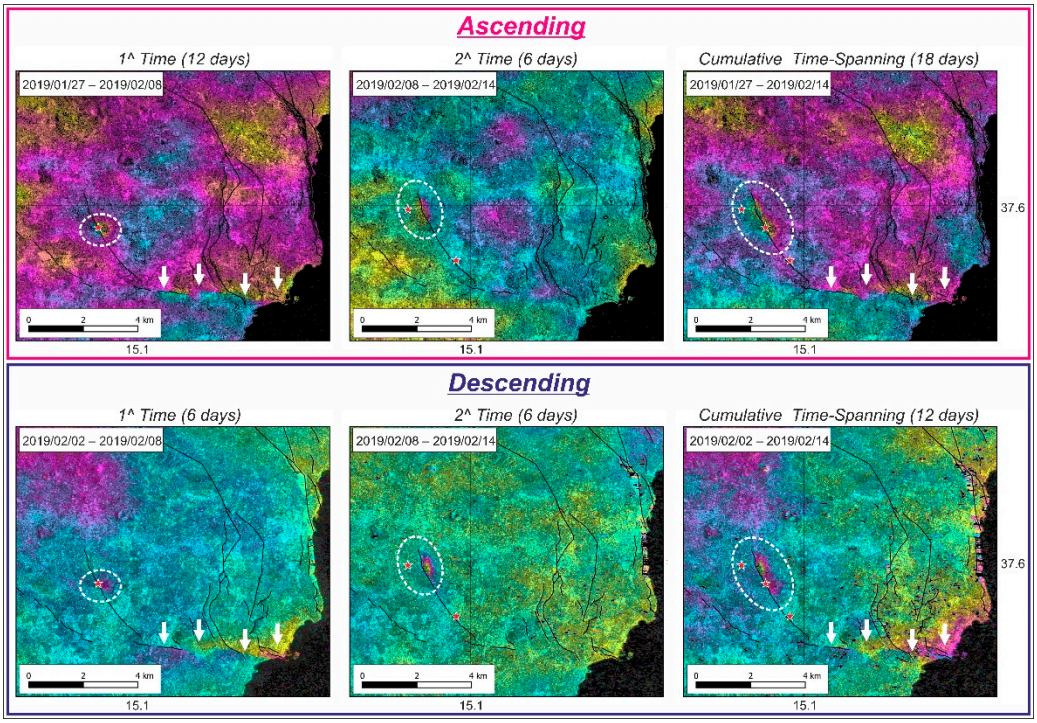

Figure 13. Ascending/descending interferogram from 27 January to 8 February 2019 (1^ time) from 8 to 14 February (2^ time) and the cumulative 27 January–14 February 2019. White arrows indicate the fault lines bounding the ground deformation features observed. For each time, the epicentrals of the seismic events are reported with red stars. The white dash circle represents the interest area.

4. Discussion

The Trecastagni Fault (TF) represents a NNW–SSE-trending active structure on Mt. Etna's southern and south-eastern flanks. It continues upwards towards a fracture system, revealed by huge fracturing in 1989, that decouples a faster, S–E-wards-moving block to the east (involving the S–E flank) from a slower southwards-moving one to the west (involving the south flank) [34,85,86].

The seismic surveys carried out on the three different areas of the TF allow us to obtain a seismostratigraphic structure of the subsoil, down to a depth of about 50 m. The surveys were performed orthogonally to the fault trace. All the sections obtained exhibit an evident depth variation of the impedance contrast (Figure 5a–c). The dislocation of the sector with the same seismic impedance allowed us to define the trend and kinematic of the tectonic lineament at depth. Moreover, observing the sections, there seems to be a correspondence between the dislocated zones in the subsoil and the fault evidence represented by visible fractures on the ground.

Observing the impedance contrast sections, it was possible to estimate the fault displacement for each investigated area. Sections 1 and 2 show a displacement of about 15–20 m, while Section 3 shows that of 10 m. Along a fault, different dislocations are usually related to the presence of asperities, local tectonic characteristics and earthquake distribution.

Considering that the areas we investigated that show nonidentical dislocations are about a hundred meters apart, this dissimilarity is probably related to the presence of lithotypes with different physical–mechanical properties [87], as evidenced by the different 1d V_s depth profiles obtained.

It is evident that TF dips towards the east, as proven by the lowered side visible in the eastern portion of the sections. Consequently, the local seismic surveys confirm that the tectonic structure is characterised by a kinematic mechanism typical of a normal fault.

Furthermore, all the polar diagrams (Figure 4b), obtained analysing the ambient seismic noise samplings, highlight an important directional effect related to the spectral peak identified in the H/V spectra. This directional effect oriented approximately WNW–ESE forms an angle of about 30–40° with the fault strike and is most likely linked with the analysed tectonic structure [88,89].

Moreover, we also analysed the earthquakes occurring in a time interval between 1980 and April 2021. The main periods of strong seismic activity were recorded between October 1983 and September 1985 and in July 2002 and October 2005. The strongest earthquakes occurred in October 2005 with a local magnitude of 3.7 and 3.8. Recently, during the last 10 years, a constant weak seismic release has been observed (September 2009, July 2014 and February 2019). These temporal clusters of seismicity are often associated with acceleration of the surface deformation, well-detected by extensometers and InSAR and levelling data that define the spatiotemporal kinematics of the fault. A joint analysis provides the constraints to define and characterise the dynamics of the fault in terms of continuous, accelerated and stick-slip displacements episodes. In general, all temporal clusters of seismicity are accompanied by local acceleration of the background aseismic creep displacements, evidenced by the extensometer plots and levelling data. The extensometer measurements carried out across the TF in the period 2005–2021 reveal that the fault is characterised by an overall continuous extension rate of about 4 cm with a rate of 2.5 mm/year; DinSAR and levelling also provide some spatial constraints, indicating how the sudden episodic dislocation affects very small patches of the fault. Sometimes, acceleration episodes seem not to be accompanied by (detectable) seismicity (as in 2016). Furthermore, during these 40 years, stick-slip seismic activity and slow-slip accelerations along the TF often occur concurrently to (e.g., 1983 and 1985 eruptions) or immediately before (e.g., 2002–2003, 2004–2005 eruptions) or after (2008, 2018 eruptions) the main lateral eruptions of the Mt. Etna volcano, as well as during the inflation phases (Figures 1a, 9, 10 and 13). Medium-term deformation of the TF has already been well characterized by Time Series derived from Advanced SAR data analyses by [28,30] and summarized in the database provided by [34], together with all geometric and kinematic information from all available literature. InSAR data, often coupled with GNSS data, also evidenced some significant relationship between magmatic and/or eruptive activity and flank dynamics, with the upper part of the TF clearly shaping the ground deformation pattern [90]. The new 2019 episode presented and investigated in this work is the most complete one, in terms of available datasets, that can be investigated to analyse the complex behaviour of the TF and make some inferences on its dynamics, in relation to the acceleration transients related to magmatic and flank activity of the volcano. Indeed, after the 2018 Mt. Etna eruption, a medium-low energy seismicity affected the Trecastagni Fault in February 2019 (Table 1), when the TF area was affected by three earthquakes occurring on February 6th (Ml = 2.5), 9th (Ml = 2.9) and 10th (Ml = 2.4) and felt by the local people.

The 6 and 9 February 2019 earthquakes were not accompanied by any deformation detectable by the extensometer positioned along the TF. Later on, after the last of the three earthquakes (10 February at 04:00 UTC), the most important episode of displacement recorded by TF extensometers since their installation in 2005 occurred. Instruments

recorded a cumulating elongation of about 11 mm in five days and a delay in the activation of the northern station of about 14 h (Figure 9).

In May 2019, levelling measured almost 5 cm of vertical displacement with respect to the previous measurement made in 2012; this is a very high value, mainly imputable to the February 2019 episode (see Figure 11), considering that the structure has an estimated slip rate of about 3–4 mm/year [8].

Clear evidence and spatial detail are provided by InSAR data (Figure 13): the interferograms highlight a northwards propagation of the dislocation along the TF between the 2 and 8 and 8 and 14 February "windows", in accordance with the extensometers' delayed accelerations.

Therefore, TF activation took place progressively through seismic releases between 6 and 10 February, due also to the match between the two (6 and 10 February, events #1 and #3) epicentre locations and the deforming areas shown by InSAR; conversely, the 2–8 February interferogram evidences a significant deformation on the southern part of the fault, where the earthquake occurred only the day after, on 9 February. Subsequently, in the period between 10 and 15 February, the deformation continued to be recorded by extensometers without relevant seismic activity (Figure 8).

This behaviour follows the intrusive event of 24 December 2018 [91,92], which immediately mobilised a block of the volcano delimited by the Fiandaca-Pennisi fault (26 December, MW = 4.9) and the Pernicana fault [24,25] and, successively, activated the adjacent block delimited by the San Gregorio and Trecastagni Faults.

Of note, starting from January 2019, the temporal distribution of the most energetic events follows an "anticlockwise" rotation from the south-western flank to the southern and eastern sectors of the volcano [24]. During the 2018 flank eruption, the magma intrusion caused significant ground deformation [91] and redistribution of stress on the neighbouring faults (Figure 12). According to Alparone et al., 2020 [24], the temporal anticlockwise distribution, from the south-western flank (Rift W) to the southern and eastern sectors of the volcano, of the most powerful events (H < 6 km) after the eruptive episode, could delimit the margins of the unstable sector [24].

Furthermore, from the distribution in depth of the earthquakes, it is clear that the TF is more seismogenic within the first 5 km of depth, where the strongest earthquakes occur mainly in the form of swarms and/or isolated shocks. This behaviour and distribution of earthquakes is similar to what was already observed along the northern boundary of the mobile flank, the Pernicana fault [7], probably related to the thickness of the pile involved in the flank dynamics and/or to the transition to a ductile deformation at depth due to a lithological change. The distribution of the magnitudes in depth (i.e., that the strongest events are shallow) could be influenced by the load of the eastern sector sliding in the shallower layers. The TF has a much lower seismic release than other active faults of Mt. Etna volcano, such as the Pernicana-Provenzana fault [24,25].

5. Conclusions

TF is a crucial tectonic structure, within Mt. Etna's dynamics, representing a part of the discontinuities bordering the sliding unstable sector that falls in a densely inhabited territory.

The seismostratigraphic structure of the subsurface clearly highlights the presence and kinematics of TF. The analysis of the geophysical survey results confirms that the different physical and mechanical features of the lithotypes characterising the subsurface affect the dislocation along TF. Moreover, this structure is associated to an important directional effect oriented about WNW–ESE, forming an angle of 30–40° with fault segment strike.

TF is seismically active up to a depth of about 5 km, while the deepest seismicity of this area is probably linked to the NNW–SSE regional trend [7].

Ground deformation and seismicity indicate how TF is characterised by a continuous aseismic dynamic that sometimes shows transient accelerations and seismic stick-slip behaviour with low-energy shallow hypocentres. This dual behaviour can be found on different patches of the fault but also in the same segment in different periods; this time–

space variability of behaviour in the same fault is not a novelty, at least on Mt. Etna faults, as reported in detail in a similar test case [35].

This is linked to Mt. Etna dynamics related to magma pressurisation and/or intrusion that induces additional stress at the periphery of the volcano, stimulating and facilitating the slip along the fault systems that dissect the mobile flanks of the edifice. The February 2019 episode suggests that TF responded with a delay of about 40 days to the stress induced by the December 2018 dike intrusion and successive eastern flank sliding acceleration [92,93].

The TF, therefore, has a key role in distributing the strain during strong and/or long-lasting inflation periods and the main intrusive events in relation to the general dynamics of the southern and eastern flanks of the volcano. Moreover, TF lies within an intensely inhabited area, hence directly impacting roads and buildings, and it is therefore crucial to improve our knowledge on its specific nature and dynamics.

Author Contributions: Conceptualization, A.U., S.A., S.G. (Sabrina Grassi), S.I., A.B., F.G., S.G. (Salvatore Gambino) and G.M.; methodology, S.A., A.U., S.G. (Sabrina Grassi), S.G. (Salvatore Gambino), S.I., A.B., F.G., G.M., F.L., G.P., L.P. and F.O.; validation, A.U., S.A., S.G. (Sabrina Grassi), S.I., A.B., F.G. and S.G. (Salvatore Gambino); formal analysis, A.U., S.A., S.G. (Sabrina Grassi), S.I., A.B., F.G., S.G. (Salvatore Gambino), G.M. and L.P.; investigation, S.A., A.U., S.G. (Sabrina Grassi), S.I., A.B., F.G., S.G. (Salvatore Gambino), G.M., L.P. and F.O.; data curation, A.U., S.A., S.G. (Sabrina Grassi), S.I., A.B., F.G., S.G. (Salvatore Gambino), G.M., L.P. and F.O.; writing—original draft preparation, S.A., A.U., S.G. (Sabrina Grassi), S.I., A.B., F.G., S.G. (Salvatore Gambino) and G.M.; writing—review and editing, S.A., A.U., S.G. (Sabrina Grassi), S.I., A.B., F.G., S.G. (Salvatore Gambino) and G.M.; supervision, S.A., A.U., S.G. (Salvatore Gambino), S.I., A.B. and F.G. All authors have read and agreed to the published version of the manuscript.

Funding: This study has been developed in the framework of the IMPACT project funded by the Istituto Nazionale di Geofisica e Vulcanologia ("Vulcani" Department). D59C19000130005.

Institutional Review Board Statement: Not applicable.

Informed Consent Statement: Not applicable.

Data Availability Statement: The data presented in this study are available on request from the corresponding author. The data are not publicly available as these are data of different types and disciplines and can thus be better requested specifically.

Acknowledgments: The authors wish to thank Gruppo Analisi Dati Sismici of Istituto Nazionale di Geofisica e Vulcanologia—Osservatorio Etneo—Sezione di Catania for providing the earthquakes catalogue. We are also indebted to the technicians of the INGV-OE seismic network staff for enabling the acquisition of seismic data. A special thanks to the Municipality of San Gregorio di Catania (CT), which enabled installing the seismic station SGR and provided considerable logistic support. We also thank Giuseppe Brandi for carrying out all levelling surveys and the INGV-OV former Director Francesca Bianco for funding them. Thanks are also due to Giuseppe Falzone, Angelo Ferro and Giuseppe Laudani for handling the INGV-OE extensometer network and S. Conway for reviewing the English text. The research activities reported in this work have been carried out also in the framework of the GEO-GSNL Mt. Etna Volcano Supersite initiative. The authors are grateful to the editor and anonymous reviewers for their constructive review that significantly improved the manuscript.

Conflicts of Interest: The authors declare no conflict of interest.

References

1. Bonaccorso, A.; Ferrucci, F.; Patanè, D.; Villari, L. Fast deformation processes and eruptive activity at Mount Etna (Italy). *J. Geophys. Res.* **1996**, *101*, 17467–17480. [CrossRef]
2. Gresta, S.; Peruzza, L.; Slejko, D.; Distefano, G. Inferences on the main volcanotectonic structures at Mt Etna (Sicily) from a probabilistic seismological approach. *J. Seismol.* **1998**, *2*, 105–116. [CrossRef]
3. De Guidi, G.; Barberi, G.; Barreca, G.; Bruno, V.; Cultrera, F.; Grassi, S.; Imposa, S.; Mattia, M.; Monaco, C.; Scarfì, L.; et al. Geological, seismological and geodetic evidence of active thrusting and folding south of Mt. Etna (eastern Sicily): Revaluation of "seismic efficiency" of the Sicilian Basal Thrust. *J. Geodyn.* **2015**, *90*, 32–41. [CrossRef]
4. De Guidi, G.; Imposa, S.; Scudero, S.; Palano, M. New evidence for Late Quaternary deformation of the substratum of Mt. Etna volcano (Sicily, Italy): Clues indicate active crustal doming. *Bull. Volcanol.* **2014**, *76*, 1–13. [CrossRef]

5. De Gori, P.; Giampiccolo, E.; Cocina, O.; Branca, S.; Doglioni, C.; Chiarabba, C. Re-pressurized magma at Mt. Etna, Italy, may feed eruptions for years. *Commun. Earth Environ.* **2021**, *2*, 1–9. [CrossRef]
6. Patanè, D.; Di Grazia, G.; Cannata, A.; Montalto, P.; Boschi, E. Shallow magma pathway geometry at Mt. Etna volcano. *Geochem. Geophys.* **2008**, *9*, 2131. [CrossRef]
7. Alparone, S.; Barberi, G.; Bonforte, A.; Maiolino, V.; Ursino, A. Evidence of multiple strain fields beneath the eastern flank of Mt. Etna volcano (Sicily, Italy) deduced from seismic and geodetic data during 2003–2004. *Bull. Volc.* **2011**, *73*, 869–885. [CrossRef]
8. Bonforte, A.; Carnazzo, A.; Gambino, S.; Guglielmino, F.; Obrizzo, F.; Puglisi, G. A multidisciplinary study of an active fault crossing urban areas: The Trecastagni Fault at Mt. Etna (Italy). *J. Volcanol. Geotherm. Res.* **2013**, *251*, 41–49. [CrossRef]
9. Poland, M.; Peltier, A.; Bonforte, A.; Puglisi, G. The spectrum of persistent volcanic flank instability; A review and proposed framework based on Kilauea, Piton de la Fournaise and Etna. *J. Volcanol. Geotherm. Res.* **2017**, *339*, 63–80. [CrossRef]
10. Borgia, A.; Ferrari, L.; Pasquarè, G. Importance of gravitational spreading in the tectonic evolution of Mount Etna. *Nature* **1992**, *357*, 231–235. [CrossRef]
11. Lo Giudice, E.; Rasà, R. Very shallow earthquakes and brittle deformation in active volcanic areas: The Etnean region as example. *Tectonophysics* **1992**, *202*, 257–268. [CrossRef]
12. Monaco, C.; Tapponnier, P.; Tortorici, L.; Gillot, P.Y. Late Quaternary slip rates on the Acireale–Piedimonte normal faults and tectonic origin of Mt Etna (Sicily). *Earth Planet. Sci. Lett.* **1997**, *147*, 125–139. [CrossRef]
13. Borgia, A.; Lanari, R.; Sansosti, E.; Tesauro, M.; Berardino, P.; Fornaro, G.; Neri, M.; Murray, J.B. Actively growing anticlines beneath Catania from the distal motion of Mount Etna's decollement measured by SAR interferometry and GPS. *Geophys. Res. Lett.* **2000**, *27*, 3409–3412. [CrossRef]
14. Neri, M.; Acocella, V.; Behncke, B. The role of the Pernicana Fault System in the spreading of Mount Etna (Italy) during the 2002–2003 eruption. *Bull. Volcanol.* **2004**, *66*, 417–430. [CrossRef]
15. Walter, T.R.; Acocella, V.; Neri, M.; Amelung, F. Feedback processes between magmatic events and flank movement at Mount Etna (Italy) during the 2002–2003 eruption. *J. Geophys. Res.* **2005**, *110*, B10. [CrossRef]
16. Rust, D.; Neri, M. The boundaries of large-scale collapse on the flanks of Mount Etna, Sicily. In Volcano Instability on the Earth and Other Planets (eds McGuire, W.J., Jones, A.P. & Neuberg, J.). *J. Geol. Soc.* **1996**, *110*, 193–208.
17. Scudero, S.; De Guidi, G.; Imposa, S.; Currenti, G. Modelling the long-term deformation of the sedimentary substrate of Mt. Etna volcano (Italy). *Terra Nova* **2015**, *27*, 338–345. [CrossRef]
18. Allard, P.; Behncke, B.; D'Amico, S.; Neri, M.; Gambino, S. Mount Etna 1993–2005: Anatomy of an evolving eruptive cycle. *Earth Sci. Rev.* **2006**, *78*, 85–114. [CrossRef]
19. Bonforte, A.; Bonaccorso, A.; Guglielmino, F.; Palano, M.; Puglisi, G. Feeding system and magma storage beneath Mt. Etna as revealed by recent inflation/deflation cycles. *J. Geophys. Res.* **2008**, *113*, 5334. [CrossRef]
20. Bonforte, A.; Gambino, S.; Guglielmino, F.; Obrizzo, F.; Palano, M.; Puglisi, G. Ground deformation modelling of flank dynamics prior to the 2002 eruption of Mt. Etna. *Bull. Volcanol.* **2007**, *69*, 757–768. [CrossRef]
21. Rasà, R.; Romano, R.; Lo Giudice, E. Morphotectonic map of Mt. Etna. Carta scala 1:100.000. *Mem. Soc. Geol. It.* **1982**, *23*, 8288.
22. Azzaro, R.; Lo Giudice, E.; Rasà, R. Il terremoto di Piano Pernicana (Etna Nord) del 28-10-1988. Campo macrosismico e quadro deformativo fragile associato all'evento. *Boll. GNV* **1988**, *5*, 22–24.
23. Acocella, V.; Neri, M. Structural features of an active strike–slip fault on the sliding flank of Mt. Etna (Italy). *J. Struct. Geol.* **2005**, *27*, 343–355. [CrossRef]
24. Alparone, S.; Cocina, O.; Ferrari, F.; Gambino, S.; Mostaccio, A.; Spampinato, S.; Tuvè, T.; Ursino, A. Seismological features of the Pernicana—Provenzana Fault System (Mt. Etna, Italy) and implications for the dynamics of the northeastern flank of the volcano. *J. Volcanol. Geotherm. Res.* **2013**, *251*, 16–26. [CrossRef]
25. Cannata, A.; Iozzia, A.; Alparone, S.; Bonforte, A.; Cannavò, F.; Cesca, S.; Gresta, S.; Rivalta, E.; Ursino, A. Repeating earthquakes and ground deformation reveal the structure and triggering mechanisms of the Pernicana fault, Mt. Etna. *Commun. Earth. Environ.* **2021**, *2*, 116. [CrossRef]
26. Neri, M.; Guglielmino, F.; Rust, D. Flank instability on Mount Etna: Radon, radar interferometry, and geodetic data from the southwestern boundary of the unstable sector. *J. Geophys. Res.* **2007**, *112*, 4756. [CrossRef]
27. Froger, J.L.; Merle, O.; Briole, P. Active spreading and regional extension at Mount Etna imaged by SAR interferometry. *Earth Planet Sci. Lett.* **2001**, *187*, 245–258. [CrossRef]
28. Bonforte, A.; Guglielmino, F.; Coltelli, M.; Ferretti, A.; Puglisi, G. Structural assessment of Mt. Etna volcano from Permanent Scatterers analysis. *Geochem. Geophys. Geosystems* **2011**, *12*, 3213. [CrossRef]
29. Neri, M.; Casu, F.; Acocella, V.; Solaro, G.; Pepe, S.; Berardino, P.; Sansosti, E.; Caltabiano, T.; Lundgren, P.; Lanari, R. Deformation and eruptions at Mt. Etna (Italy): A lesson from 15 years of observations. *Geophys. Res. Lett.* **2009**, *36*, 151. [CrossRef]
30. Solaro, G.; Acocella, V.; Pepe, S.; Ruch, J.; Neri, M.; Sansosti, E. Anatomy of an unstable volcano from InSAR: Multiple processes affecting flank instability at Mt. Etna, 1994–2008. *J. Geophys. Res.* **2010**, *115*, B10405. [CrossRef]
31. Gambino, S.; Bonforte, A.; Carnazzo, A.; Falzone, G.; Ferrari, F.; Ferro, A.; Guglielmino, F.; Laudani, G.; Maiolino, V.; Puglisi, G. Displacement across the Trecastagni Fault (Mt. Etna) and induced seismicity: The October 2009–January 2010 episode. *Ann. Geophys.* **2011**, *54*, 414–423.
32. Urlaub, M.; Geersen, J.; Petersen, F.; Gross, F.; Bonforte, A.; Krastel, S.; Kopp, H. The Submarine Boundaries of Mount Etna's Unstable Southeastern Flank. *Front. Earth Sci.* **2022**, *10*, 810790. [CrossRef]

33. Urlaub, M.; Petersen, F.; Gross, F.; Bonforte, A.; Puglisi, G.; Guglielmino, F.; Krastel, S.; Lange, D.; Kopp, H. Gravitational collapse of Mount Etna's southeastern flank. *Sci. Adv.* **2018**, *4*, eaat9700. [CrossRef]
34. Barreca, G.; Bonforte, A.; Neri, M. A pilot GIS database of active faults of Mt. Etna (Sicily): A tool for integrated hazard evaluation. *J. Volcanol. Geotherm. Res.* **2013**, *251*, 170–186. [CrossRef]
35. Azzaro, R.; Bonforte, A.; D'Amico, S.; Guglielmino, F.; Scarfì, L. Stick-slip vs. stable sliding fault behaviour: A case-study using a multidisciplinary approach in the volcanic region of Mt. Etna (Italy). *Tectonophysics* **2020**, *790*, 228554. [CrossRef]
36. Alparone, S.; Barberi, G.; Giampiccolo, E.; Maiolino, V.; Mostaccio, A.; Musumeci, C.; Scaltrito, A.; Scarfì, L.; Tuvè, T.; Ursino, A. Seismological constraints on the 2018 Mt. Etna (Italy) flank eruption and implications for the flank dynamics of the volcano. *Terra Nova* **2020**, *32*, 334–344. [CrossRef]
37. Cosentino, M.; Lombardo, G.; Patane, G.; Schick, G.; Sharp, A.L. Seismological researches on Mount Etna: State of art and recent trends. *Mem. Soc. Geol. It.* **1982**, *23*, 159–202.
38. Gresta, S.; Patanè, G. Review of seismological studies at Mount Etna. *Pure Appl. Geophys.* **1987**, *125*, 951–970. [CrossRef]
39. Patanè, D.; Cocina, O.; Falsaperla, S.; Privitera, E.; Spampinato, S. Mt Etna Volcano: A Seismological Framework. In *Etna Volcano Laboratory*; Bonaccorso, A., Calvari, S., Coltelli, M., Del Negro, C., Falsaperla, S., Eds.; AGU BOOK (Geophysical Monograph Series); Wiley: Washington, DC, USA, 2004; Volume 4, pp. 147–165. [CrossRef]
40. Carnazzo, A.; Ferro, A.; Falzone, G.; Gambino, S.; Laudani, G. *La Rete Estensimetrica della Faglia di Trecastagni*; INGV Rapporto Tecnico no. 56; INGV Publication: Rome, Italy, 2006.
41. Aiesi, G.; Bonforte, A.; Brandi, G.; Calvagna, F.; Consoli, S.; Distefano, G.; Falzone, G.; Ferro, A.; Gambino, S.; Guglielmino, F.; et al. Dynamics of the Boundaries of the Mt. Etna Sliding Flanks: The Multidisciplinary Study of the Pernicana and Trecastagni Faults. Abstract Conferenza, A. Rittmann. 2020. Available online: https://www.conferenzarittmann.it/images/2020/Miscellanea_52.pdf (accessed on 20 July 2022).
42. Obrizzo, F.; Pingue, F.; Troise, C.; De Natale, G. Bayesian inversion of 1994–1998 vertical displacements at Mt Etna: Evidence for magma intrusion. *Geophys. J. Int.* **2004**, *157*, 935–946. [CrossRef]
43. Obrizzo, F.; Pingue, F.; Troise, C.; De Natale, G. Coseismic displacements and creeping along the Pernicana fault (Etna, Italy) in the last 17 years: A detailed study of a tectonic structure on a volcano. *J. Volcanol. Geotherm. Res.* **2001**, *109*, 109–131. [CrossRef]
44. Italiana Commissione Geodetica. Guida alla progettazione e all'esecuzione delle livellazioni geometriche. *Boll. Geod. Sci. Aff.* **1975**, *34*, 1.
45. Bomford, G. *Geodesy*; Oxford University Press: New York, NY, USA, 1971.
46. Wegmüller, U.; Werner, C.; Strozzi, T.; Wiesmann, A.; Frey, O.; Santoro, M. Sentinel-1 IWS mode support in the GAMMA software. In Proceedings of the 2015 IEEE 5th Asia-Pacific Conference on Synthetic Aperture Radar (APSAR), Singapore, 1–4 September 2015; Volume 4, pp. 431–436. [CrossRef]
47. Jarvis, A.; Reuter, H.I.; Nelson, A.; Guevara, E. Hole-filled SRTM for the globe Version 4, available from the CGIAR-CSI SRTM 90m Database. 2008. Available online: https://srtm.csi.cgiar.org/ (accessed on 20 July 2022).
48. Park, C.B.; Miller, R.D.; Xia, J. Multichannel analysis of surface waves. *Geophysics* **1999**, *64*, 800–808. [CrossRef]
49. Nogoshi, M.; Igarashi, T. On the propagation characteristics estimations of subsurface using microtremors on the ground suface. *J. Seismol. Soc. Jpn.* **1970**, *23*, 264–280.
50. Nakamura, Y. A method for dynamic characteristics estimation of subsurface using microtremor on the ground surface. *QR Railway Tech. Res. Inst.* **1989**, *30*, 25–33.
51. Okada, H.; Suto, K. *The Microtremor Survey Method*; Society of Exploration Geophysicists: Houston, TX, USA, 2003.
52. Yamanaka, H.; Takemura, M.; Ishida, H.; Niwa, M. Characteristics of long-period microtremors and their applicability in exploration of deep sedimentary layers. *Bull. Seismol. Soc. Am.* **1994**, *84*, 1831–1841. [CrossRef]
53. Parolai, S.; Bormann, P.; Milkereit, C. New relationships between Vs, thickness of sediments and resonance frequency calculated from H/V ratio of seismic noise for the Cologne area. *Bull. Seismol. Soc. Am.* **2002**, *92*, 2521–2527. [CrossRef]
54. Imposa, S.; Coco, G.; Corrao, M. Site effects close to structural lineaments in eastern Sicily (Italy). *Eng. Geol.* **2004**, *72*, 331–341. [CrossRef]
55. Castellaro, S.; Mulargia, F.; Bianconi, L. Passive Seismic Stratigraphy: A new efficient, fast and economic technique. *J. Geotech. Environ. Geol.* **2005**, *3*, 51–77.
56. Martorana, R.; Agate, M.; Capizzi, P.; Cavera, F.; D'Alessandro, A. Seismostratigraphic model of "La Bandita"area in the Palermo Plain (Sicily, Italy) through HVSR inversion constrained by stratigraphic data. *Ital. J. Geosci.* **2018**, *137*, 73–86. [CrossRef]
57. Imposa, S.; Grassi, S.; Fazio, F.; Rannisi, G.; Cino, P. Geophysical surveys to study a landslide body (North-Eastern Sicily). *Nat. Hazards* **2017**, *86*, 327–343. [CrossRef]
58. Imposa, S.; Panzera, F.; Grassi, S.; Lombardo, G.; Catalano, S.; Romagnoli, G.; Tortorici, G. Geophysical and geologic surveys of the areas struck by the August 26th 2016 Central Italy earthquake: The study case of Pretare and Piedilama. *J. Appl. Geophys.* **2017**, *145*, 17–27. [CrossRef]
59. Imposa, S.; Grassi, S.; De Guidi, G.; Battaglia, F.; Lanaia, G.; Scudero, S. 3D subsoil model of the San Biagio 'Salinelle' mud volcanoes (Belpasso, SICILY) derived from geophysical surveys. *Surv. Geophys.* **2016**, *37*, 1117–1138. [CrossRef]
60. Imposa, S.; Motta, E.; Capilleri, P.; Imposa, G. HVSR and MASW seismic survey for characterizing the local seismic response: A case study in Catania area (Italy). In Proceedings of the 1st IMEKO TC-4 International Workshop on Metrology for Geotechnics, Benevento, Italy, 17–18 March 2016.

61. Pappalardo, G.; Mineo, S.; Imposa, S.; Grassi, S.; Leotta, A.; La Rosa, F.; Salerno, D. A quick combined approach for the characterization of a cliff during a post-rockfall emergency. *Landslides* **2020**, *17*, 1063–1081. [CrossRef]
62. Pappalardo, G.; Imposa, S.; Barbano, M.S.; Grassi, S.; Mineo, S. Study of landslides at the archaeological site of Abakainon necropolis (NE Sicily) by geomorphological and geophysical investigations. *Landslides* **2018**, *15*, 1279–1297. [CrossRef]
63. Grassi, S.; De Guidi, G.; Patti, G.; Brighenti, F.; Carnemolla, F.; Imposa, S. 3D subsoil reconstruction of a mud volcano in central Sicily by means of geophysical surveys. *Acta Geophys.* **2022**, *2*, 00774. [CrossRef]
64. Grassi, S.; Patti, G.; Tiralongo, P.; Imposa, S.; Aprile, D. Applied geophysics to support the cultural heritage safeguard: A quick and non-invasive method to evaluate the dynamic response of a great historical interest building. *J. Appl. Geophys.* **2021**, *189*, 104321. [CrossRef]
65. Grassi, S.; Imposa, S.; Patti, G.; Boso, D.; Lombardo, G.; Panzera, F. Geophysical surveys for the dynamic characterization of a cultural heritage building and its subsoil: The S. Michele Arcangelo Church (Acireale, eastern Sicily). *J. Cult. Herit.* **2019**, *36*, 72–84. [CrossRef]
66. Ibs-von Seht, M.; Wohlenberg, J. Microtremor measurements used to map thickness of soft sediments. *Bull. Seismol. Soc. Am.* **1999**, *89*, 250–259. [CrossRef]
67. Branca, S.; Coltelli, M.; Groppelli, G.; Lentini, F. Geological map of Etna volcano, 1:50,000 scale. *Ital. J. Geosci.* **2011**, *130*, 265–291. [CrossRef]
68. Azzaro, R. Earthquake Surface Faulting at Mount Etna Volcano (Sicily) And Implications for Active Tectonics. *J. Geodyn.* **1999**, *28*, 193–213. [CrossRef]
69. Azzaro, R.; D'Amico, S. *Catalogo Macrosismico dei Terremoti Etnei dal 1832 al 2005*; INGV-CT; INGV Publication: Rome, Italy, 2008.
70. Distefano, G.; Di Grazia, G. *Database Localizzazioni Ipocentrali Terremoti Etna dal 1977 al 2001*; Progetto DPC-INGV; INGV Publication: Rome, Italy, 2005; Volume 3, pp. 2004–2006.
71. Alparone, S.; Maiolino, V.; Mostaccio, A.; Scaltrito, A.; Ursino, A.; Barberi, G.; D'Amico, S.; Di Grazia, G.; Giampiccolo, E.; Musumeci, C.; et al. Instrumental seismic catalogue of Mt. Etna earthquakes (Sicily, Italy): Ten years (2000–2010) of instrumental recordings. *Ann. Geophys.* **2015**, *58*, 6591. [CrossRef]
72. Alparone, S.C.; Barberi, G.; Di Grazia, G.; Giampiccolo, E.; Maiolino, V.; Mostaccio, A.; Musumeci, C.; Scaltrito, A.; Ursino, A. *Mt. Etna Seismic Catalog 2011–2013 (Version 1) [Data Set]*; INGV Publication: Rome, Italy, 2020. [CrossRef]
73. Alparone, S.C.; Barberi, G.; Di Grazia, G.; Giampiccolo, E.; Maiolino, V.; Mostaccio, A.; Musumeci, C.; Scaltrito, A.; Tuvè, T.; Ursino, A. *Mt. Etna Seismic Catalog 2014–2016 (Version 1) [Data Set]*; INGV Publication: Rome, Italy, 2020. [CrossRef]
74. Alparone, S.C.; Barberi, G.; Di Grazia, G.; Ferrari, F.; Giampiccolo, E.; Maiolino, V.; Mostaccio, A.; Musumeci, C.; Scaltrito, A.; Tuvè, T.; et al. *Mt. Etna Revised and Concise Seismic Catalog from 1999 (EtnaRCSC) [Data Set]*; INGV Publication: Rome, Italy, 2020. [CrossRef]
75. Alparone, S.; Barberi, G.; Di Grazia, G.; Giampiccolo, E.; Maiolino, V.; Mostaccio, A.; Musumeci, C.; Scaltrito, A.; Tuvè, T.; Ursino, A. *Mt. Etna Seismic Catalog 2017–2019 (EtnaSC_2017_2019) (Version 1) [Data Set]*; INGV Publication: Rome, Italy, 2022. [CrossRef]
76. Barberi, G.; Di Grazia, G.; Ferrari, F.; Giampiccolo, E.; Maiolino, V.; Mostaccio, A.; Musumeci, C.; Scaltrito, A.; Sciotto, M.; Tusa, G.; et al. *Mt. Etna Revised Seismic Catalog from 2020 (EtnaRSC2020) (Version 1) [Data Set]*; INGV Publication: Rome, Italy, 2020. [CrossRef]
77. Rydelek, P.A.; Sacks, I.S. Testing the completeness of earthquake catalogues and the hypothesis of self-similarity. *Nature* **1989**, *337*, 251–253. [CrossRef]
78. Wiemer, S.; Wyss, M. Minimum magnitude of completeness in earthquake catalogues: Examples from Alaska, the Western United States, and Japan. *Bull. Seismol. Soc. Am.* **2000**, *90*, 859–869. [CrossRef]
79. Wiemer, S.A. Software package to analyze seismicity: ZMAP. *Seismol. Res. Lett.* **2001**, *72*, 373–382. [CrossRef]
80. Richter, C.F. *Elementary Seismology*; W. H. Freeman and Co.: San Francisco, CA, USA, 1958.
81. Lahr, J.C. *Hypoellipse/Version 2.0*: A Computer Program for Determining Local Earthquake Hypocentral Parameters, Magnitude, and First Motion Pattern*; U.S. Geological Survey: Reston, VA, USA, 1989; pp. 89–116. [CrossRef]
82. Lee, W.H.K.; Lahr, J.C. *HYPO71: A Computer Program for Determining Hypocenter, Magnitude, and First Motion Pattern of Local Earthquakes*; OFR; U.S. Geological Survey: Reston, VA, USA, 1975.
83. Hirn, A.; Nercessian, A.; Sapin, M.; Ferrucci, F.; Wittlinger, G. Seismic heterogeneity of Mt Etna: Structure and activity. *Geophys. J. Int.* **1991**, *105*, 139–153. [CrossRef]
84. Patanè, D.; Ferrucci, F.; Gresta, S. Spectral features of microearthquakes in volcanic areas: Attenuation in the crust and amplitude response of the site at Mt. Etna, Italy. *Bull. Seismol. Soc. Am.* **1994**, *84*, 1842–1860. [CrossRef]
85. Bonforte, A.; Fanizza, G.; Greco, F.; Matera, A.; Sulpizio, R. Long-term dynamics across a volcanic rift: 21 years of microgravity and GPS observations on the southern flank of Mt. Etna volcano. *J. Volcanol. Geotherm. Res.* **2017**, *344*, 174–184. [CrossRef]
86. Bonforte, A.; Gambino, S.; Neri, M. Intrusion of eccentric dikes: The case of the 2001 eruption and its role in the dynamics of Mt. Etna volcano. *Tectonophysics* **2009**, *471*, 78–86. [CrossRef]
87. Gudmundsson, A. Effects of Young's modulus on fault displacement. *Cr. Geosci.* **2004**, *336*, 85–92. [CrossRef]
88. Rigano, R.; Cara, F.; Lombardo, G.; Rovelli, A. Evidence for ground motion polarization on fault zones of Mount Etna volcano. *J. Geophys. Res. Solid Earth* **2008**, *113*, 5574. [CrossRef]
89. Di Giulio, G.; Cara, F.; Rovelli, A.; Lombardo, G.; Rigano, R. Evidences for strong directional resonances in intensely deformed zones of the Pernicana fault, Mount Etna, Italy. *J. Geophys. Res. Solid Earth* **2009**, *114*, B10. [CrossRef]

90. Bonforte, A.; Guglielmino, F.; Puglisi, G. Interaction between magma intrusion and flank dynamics at Mt. Etna in 2008, imaged by integrated dense GPS and DInSAR data. *Geochem. Geophys. Geosys.* **2013**, *14*, 2818–2835. [CrossRef]
91. Bonforte, A.; Guglielmino, F.; Puglisi, G. Large dyke intrusion and small eruption: The December 24, 2018 Mt. Etna eruption imaged by Sentinel-1 data. *Terra Nova* **2019**, *5*, 12403. [CrossRef]
92. Aloisi, M.; Bonaccorso, A.; Cannavò, F.; Currenti, G.; Gambino, S. The 24 December 2018 eruptive intrusion at Etna volcano as revealed by multidisciplinary continuous deformation networks (CGPS, borehole, strainmeters and tiltmeters). *J. Geophy. Res. Solid Earth* **2020**, *125*, 9117. [CrossRef]
93. Gambino, S.; Distefano, G. Intrusive Seismic Swarms as Possible Precursors of Destructive Earthquakes on Mt. Etna's Eastern Flank. *Int. J. Geoph.* **2022**, *2022*, 8565536. [CrossRef]